Transcutaneous Measurement and Spectrum Analysis of Heart Wall Vibrations

Hiroshi Kanai, *Member, IEEE,* Michie Sato, Yoshiro Koiwa, and Noriyoshi Chubachi, *Member, IEEE*

Abstract—For the noninvasive diagnosis of heart disease based on the acoustic and elastic characteristics of the heart muscle, it is necessary to transcutaneously measure small *vibration* signals, including components with an amplitude of less than 100 μm, from various parts of the heart wall continuously for periods of more than several heartbeats in a wide frequency range up to 1 kHz. Such measurement, however, has not been realized by any ultrasonic diagnostic methods or systems to date. By introducing the constraint least-square approach, this paper proposes a new method for accurately tracking the movement of the heart wall based on both the phase and magnitude of the demodulated signal to determine the instantaneous position of the object so that the *vibration* velocity of the moving object can be accurately estimated. By this method, small *vibrations* of the heart wall with small amplitudes less than 100 μm on the *motion* resulting from a heartbeat with large amplitude of 10 mm can be successfully detected with sufficient reproducibility in the frequency range up to several hundred Hertz continuously for periods of about 10 heartbeats. The resultant small vibration is analyzed not only in the time domain, but also in the frequency domain. As confirmed by the preliminary experiments herein reported, the new method offers potential for research in acoustical diagnosis of heart disease.

I. INTRODUCTION

TO diagnose the cardiovascular system based on the acoustic characteristics of the myocardium or the arterial walls, it is necessary to measure small *vibration* signals on these walls in a wide frequency range and to accurately analyze the spectrum of the resultant waveform. For the latter purpose of spectrum analysis, we have already developed a method for estimating the spectral transition of heart sounds between short-length signals of succeeding frames in low SNR cases [1]. By applying this method to the analysis of multiframe signals of the fourth heart sound obtained during a stress test, significant differences between the spectral transition patterns of 10 patients with myocardial infarction and 10 normal subjects were clearly detected. However, when measuring a heart sound from the chest wall of a patient, it is difficult to avoid the influence of the transfer characteristics of the lung. Thus, the heart sounds were detected by an accelerometer placed in the esophagus [1]. However, esophageal probe placement is not well tolerated in unanesthetized patients. Moreover, it is difficult to detect local *vibrations* of small areas of various parts of the ventricle wall with such placement. It is, therefore, desirable to use a probe placed on the chest wall to transcutaneously detect small *vibrations* for each local area by means of ultrasound.

Since *motion* detection based on the continuous-wave ultrasonic Doppler method was first demonstrated [2], numerous elaborate techniques have been proposed for acoustic measurement of the velocity of the blood flow in the heart or the arteries based on the Doppler effect [3]–[11].

However, to measure heart wall *vibration* signals with small amplitudes (less than ± 100 μm) up to at least a few hundred Hertz, the *vibrations* are superimposed on the *motion* with large amplitudes (about ± 10 mm) of several Hertz resulting from the heartbeat during one cardiac cycle. Thus, there are large fluctuations (about ± 8 μs) in the transit period of an ultrasonic wave traveling from a transducer to the heart wall and back during the period of one heartbeat. It is, therefore, necessary to accurately identify the instantaneous position of the heart wall.

In this paper, the term "vibration" is employed to describe the rapid motion of the heart wall with small amplitude including high-frequency components, which is difficult to recognize by M (motion)-mode echocardiography. Thus, a *vibration* is distinguished from a *motion* with large amplitude and low frequency, the displacement of which can be displayed in the M-mode image. A small *vibration* on the heart wall, which is measured up to several hundred Hertz in this paper, is analyzed not only in the time domain, but also in the frequency domain, whereas the *motion* of the tissue or organs depicted in standard echocardiography is analyzed only in the time domain because it has only low-frequency components.

Various ultrasonic techniques for measurement of the *motion* of tissue or organs using ultrasound have been reported in the literature. The most widely employed technique is M-mode echocardiography, in which the amplitude of each ultrasonic pulse shows the slow *motion* of the structure along the ultrasonic beam. However, the spatial resolution is limited to several wavelengths, namely, more than 1 mm for ultrasound of 3 MHz. The limit is determined by the length of the ultrasonic RF pulse radiated by the ultrasonic transducer. Moreover, to determine the displacement of organs as waveforms to be analyzed, it is necessary to trace the resultant wall *motion*. However, this is not easily realized.

Several methods have been developed to measure changes in the diameter of the arterial walls by tracking arterial

H. Kanai, M. Sato, and N. Chubachi are with the Department of Electrical Engineering, Faculty of Engineering, Tohoku University, Sendai 980-77 Japan (e-mail: hkanai@chubachi.ecei.tohoku.ac.jp).

Y. Koiwa is with the First Department of Internal Medicine, School of Medicine, Tohoku University, Sendai 980-77 Japan.

wall *motion*, including only low-frequency components with small amplitudes for detection of blood flow [12], [13], for evaluation of elastic properties of the arterial walls [14]–[16], for measurement of pressures [17], and for monitoring fetal breathing [18].

A method has also been proposed and applied to measure arterial wall *motion* having large amplitudes in which the zero-crossing point of the echo signal from an arterial wall is tracked for each transmitted RF pulse using the phase-locked loop (PLL) technique [19]–[26]. In the method using the PLL circuit, however, only the phase of the received RF signal is considered and it is easily affected by additive noise as pointed out in [27]. With each of these devices using the PLL technique, experiments have shown that it is difficult to lock onto and remain locked to the desired echo [27]. However, the reason has not been considered theoretically. As will be pointed out in Section II-D of this paper, this method has an essential drawback in that the displacement is coarsely digitized at the sampling rate determined by the clock frequency employed in the PLL circuit. An alternative open-loop approach has been developed recently in which the phase is detected at a fixed distance from the transducer to trace the *motion* of the layers [27]–[29]. In these methods, an ultrasonic transducer is directly attached to the epicardium.

Since the amplitude of the motion of the vessel walls is not so large, the walls do not deviate from the selected sample volumes during the cardiac cycle. For an artery with low elasticity, however, the vessel walls deviate from the selected sample volume. This disadvantage has been overcome by letting the sample volume track the vessel walls based on the assessed displacement [30]. The displacement waveforms and the distension waveforms of the arterial walls are obtained and then analyzed in the time domain. However, transcutaneous measurement of the velocity signal on the heart wall has not yet been realized. Moreover, the obtained waveforms have not yet been analyzed as to their spectrum in the frequency domain.

We have proposed, therefore, a noninvasive transcutaneous method for measuring small *vibrations* on a local area of the heart wall [32]. The demodulated signal of the received signal is A/D converted at a sampling frequency of 1 MHz. From the phase of the received echoes, a small *vibration* signal is measured noninvasively using the ultrasonic Doppler method. In this method, however, the object position is determined only from the local maximum of the magnitude in the demodulated received echo, and the spatial resolution in the tracking of the object position highly depends on the sampling period of the demodulated received signal.

This paper proposes a new method for accurately tracking the heart wall movement using both the phase and magnitude of the digitized demodulated signal to determine the instantaneous position of the heart wall, after which the velocity signal is estimated. The resultant small vibration is analyzed not only in the time domain, but also in the frequency domain. After evaluating the validity of the proposed method by experiments using a water tank, the proposed method is applied to the *in vivo* detection of small *vibration* signals on the heart walls in
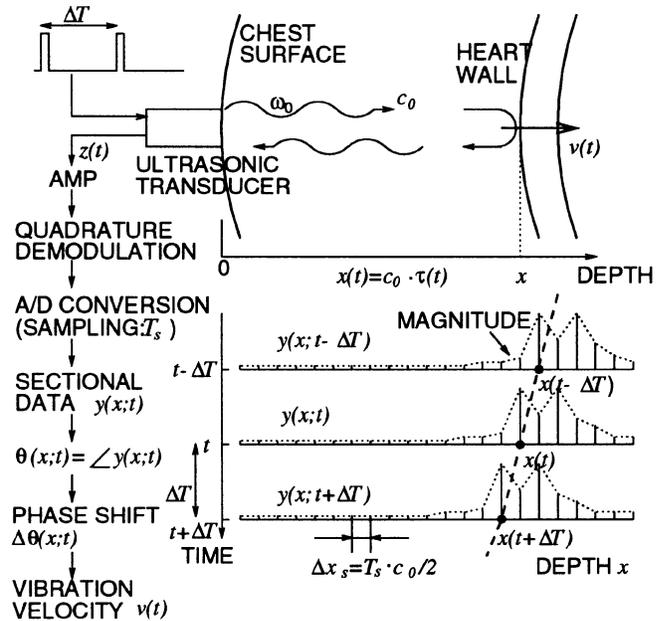

Fig. 1. Schematic representation of the transcutaneous measurement of a heart wall vibration, $v(t)$, from the chest wall using pulsive ultrasound based on the standard procedure when the object position does not vary so much.

RF pulses with angular-frequency $\omega_0 = 2\pi f_0$ are transmitted at a time interval of ΔT from an ultrasonic transducer on the chest surface. The ultrasonic pulse reflected by the heart wall is received by the same ultrasonic transducer. The output signal, $z(t)$, is amplified and quadrature demodulation is applied to the signal. The resultant complex signal is A/D converted at a sampling period of T_s and then separated into response signals $\{y(x; t)\}$ for each transmitted pulse at a time t, where x denotes the distance of the object from the ultrasonic transducer and where the spatial resolution Δx_s in the depth direction is equal to $T_s \cdot c_0/2$. Since the phase $\theta(x; t)$ of the resultant sectional complex signal $y(x; t)$ is given by $2\omega_0 x(t)/c_0$, from the phase difference $\Delta\theta(x; t)$ between the demodulated signals $y(x; t)$ and $y(x; t + \Delta T)$ of the received signals for the successively transmitted pulses in the interval ΔT, the average velocity $v(t)$ of the object during the period ΔT is given.

humans in order to show the possibility of acoustic diagnosis of the myocardium.

II. PRINCIPLE OF MEASUREMENT OF SMALL VIBRATIONS ON A MOVING OBJECT

A. Standard Velocity Measurement

RF pulses with angular-frequency $\omega_0 = 2\pi f_0$ are transmitted at a time interval of ΔT from an ultrasonic transducer on the chest surface as shown in Fig. 1. Defining the acoustic velocity as c_0, the instantaneous distance of a moving object from the ultrasonic transducer is denoted by $x(t) = c_0 \cdot \tau(t)$, where $\tau(t)$ is the instantaneous period required for one-way transmission from the ultrasonic transducer to the object. The ultrasonic pulse reflected by the object is received by the same ultrasonic transducer. The output signal, $z(t)$, is amplified and quadrature demodulation is applied to the signal. The resultant complex signal is A/D converted at a sampling period of T_s and then separated into the response signals $\{y(x; t)\}$ for each transmitted pulse at a time t, where x denotes the distance of the object from the ultrasonic transducer, and the spatial resolution Δx_s in the depth direction is equal to $T_s \cdot c_0/2$ as shown in Fig. 1.

The phase $\theta(x; t)$ of the resultant sectional complex signal $y(x; t)$ is given by the angular frequency ω_0 multiplied by twice the delay time $\tau(t)$ in the one-way propagation from the ultrasonic transducer to the object as follows:

$$\theta(x; t) = 2\omega_0\tau(t)$$
$$= 2\omega_0 \frac{x(t)}{c_0}. \tag{1}$$

The phase difference $\Delta\theta(x; t)$ between the demodulated signals $y(x; t)$ and $y(x; t + \Delta T)$ of the received signals for the successively transmitted pulses in the interval ΔT is given by

$$\Delta\theta(x; t) = \theta(x; t + \Delta T) - \theta(x; t)$$
$$= \frac{2\omega_0}{c_0} \Delta x(t) \tag{2}$$

where $\Delta x(t) = x(t + \Delta T) - x(t)$ is the movement of the object in the period ΔT at a time t, where it can be assumed that the received interval almost coincides with the transmitted interval ΔT of the ultrasonic RF pulses. By dividing the movement Δx by the period ΔT, the average velocity, denoted by $\hat{v}(t + \Delta T/2)$, of the object during the period ΔT is given by the phase difference $\Delta\theta(x; t)$ between the successively demodulated signals $y(x; t)$ and $y(x; t + \Delta T)$ as follows:

$$\hat{v}\left(t + \frac{\Delta T}{2}\right) = \frac{\Delta x(t)}{\Delta T}$$
$$= c_0 \cdot \frac{\Delta\theta(x; t)}{2\omega_0 \cdot \Delta T}. \tag{3}$$

This standard procedure can be employed only when the object position $x(t)$ does not vary much.

B. Tracking Object Position Using the Standard Cross-Correlation Function

Since the object position $x(t)$ changes by more than 10 mm, for example, for the heart wall during one heartbeat period, it is necessary to accurately track the instantaneous position $x(t)$ of the object for estimation of the *vibration* signal $v(t)$ of the object. The transmitted ultrasonic pulse has a finite length of several microseconds when the ultrasonic frequency is several megahertz. Thus, there is a pulse train consisting of a few discrete points at which each reflective signal has large magnitude as shown in the right-hand side of Fig. 1. Therefore, it is not easy to determine the object position $x(t)$ from the magnitude of the demodulated signal $y(x; t)$. Moreover, there is a large phase difference between the adjacent points in a train when the object is moving. Thus, an error in the determination of the object position introduces a large error into the resultant *vibration* signal $\hat{v}(t)$ in (3). Therefore, it is essential to accurately determine the instantaneous object position $x(t)$.

In this paper, in order to accurately determine both phase shift $\Delta\theta(x; t)$ during the period ΔT and the instantaneous object position $x(t)$, the following complex correlation is introduced in the determination procedure of the movement, δ_x, of the object position $x(t)$ from the preceding sectional data during the period ΔT.

At first, based on the standard least-square method, let us define the normalized mean squared difference between the demodulated complex signal $y(x + \delta_x; t + \Delta T)$ and the preceding signal $y(x; t)$ by $\alpha_n(\beta_n; \delta_x)$

$$\alpha_n(\beta_n; \delta_x) = \frac{\displaystyle\sum_{x \in R} |y(x + \delta_x; t + \Delta T) - \beta_n(\delta_x)y(x; t)|^2}{\dfrac{\displaystyle\sum_{x \in R} \{|y(x + \delta_x; t + \Delta T)|^2 + |y(x; t)|^2\}}{2}} \tag{4}$$

where δ_x is the movement, to be determined, of the object during the period ΔT of the succeeding pulses, R is the range $x(t) \pm \Delta x$ around the previous object-position $x(t)$ where the above difference is evaluated, and $\beta_n(\delta_x)$ is the change in complex amplitude from $y(x; t)$ to $y(x + \delta_x; t + \Delta T)$. The range $2\Delta x$ corresponds to the length of the RF pulse transmitted from the ultrasonic transducer. From (A9) in Appendix A, the minimization of $\alpha_n(\beta_n; \delta_x)$ is achieved by

$$\hat{\beta}_n(\delta_x) = \frac{\displaystyle\sum_{x \in R} y^*(x; t) \cdot y(x + \delta_x; t + \Delta T)}{\displaystyle\sum_{x \in R} |y(x; t)|^2} \tag{5}$$

where * denotes the complex conjugate. For this value of $\hat{\beta}_n(\delta_x)$, the minimum $\alpha_{n\,\mathrm{MIN}}(\delta_x)$ is given by

$$\alpha_{n\,\mathrm{MIN}}(\delta_x)$$
$$\stackrel{\mathrm{def}}{=} \min_\beta \alpha_{n\,\mathrm{MIN}}(\beta_n; \delta_x)$$
$$= \frac{\displaystyle\sum_{x \in R} |y(x; t)|^2 - \frac{\left|\displaystyle\sum_{x \in R} y^*(x; t) \cdot y(x + \delta_x; t + \Delta T)\right|}{\displaystyle\sum_{x \in R} |y(x; t)|^2}}{\dfrac{\displaystyle\sum_{x \in R} \{|y(x; t)|^2 + |y(x + \delta_x; t + \Delta T)|^2\}}{2}} \tag{6}$$

from (A11) in Appendix A. The term $\left|\sum_{x \in R} y^*(x; t) \cdot y(x + \delta_x; t + \Delta T)\right|$ in the numerator of (6) corresponds to the magnitude of the complex cross-correlation function between $y(x; t)$ and $y(x; t + \Delta T)$.

However, when the received complex signals $y(x; t)$ and $y(x; t + \Delta t)$ are described by the damped sinusoidal signals as shown in Fig. 2, the above standard correlation procedure does not uniquely determine the delay δ_x of the signal $y(x; t + \Delta t)$ from $y(x; t)$ as described below. Let us assume that the received complex signals $y(x; t)$ and $y(x; t + \Delta t)$ are digitized and are given by the following simple model:

$$y_1(n) \stackrel{\mathrm{def}}{=} y(x; t)|_{x \leftarrow n}$$
$$= z_0^n \cdot w(n) \tag{7}$$
$$y_2(n) \stackrel{\mathrm{def}}{=} y(x; t + \Delta T)|_{x \leftarrow n}$$
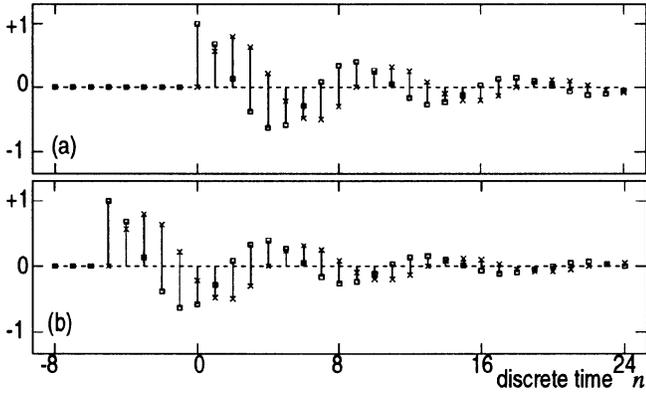$$= z_0^{n+n_0} \cdot w(n + n_0) \tag{8}$$

Fig. 2. The waveforms of a simple model of the received complex signals $y(x; t)$ and $y(x; t + \Delta T)$. The real and imaginary components are indicated by $\square$ and $\times$, respectively. (a) $y_1(n) \stackrel{\text{def}}{=} y(x; t)|_{x=n} = z_0^n \cdot w(n) = e^{-0.1n}\{\cos(2\pi n/9) + j\sin(2\pi n/9)\} \cdot w(n)$ in (7). (b) $y_2(n) \stackrel{\text{def}}{=} y(x; t + \Delta T)|_{x=n} = z_0^{n+n_0} \cdot w(n+n_0) = e^{-0.1(n+5)}\{\cos[2\pi(n+5)/9] + j\sin[2\pi(n+5)/9]\} \cdot w(n+5)$ in (8).

where z_0 is the complex constant, $-n_0$ is the delay of $y_2(n)$ from $y_1(n)$, and $w(n)$ is the step function defined by

$$w(n) = \begin{cases} 1 & n \geq 0 \\ 0 & n < 0. \end{cases} \tag{9}$$

When z_0 is $\exp(-0.1+j2\pi/9)$ and $n_0 = 5$, the waveforms of $y_1(n)$ and $y_2(n)$ are shown in Fig. 2(a) and (b), respectively. For this simple model, the minimum $\alpha_{n\,\text{MIN}}(\delta_n)$ in (6) of the normalized mean squared difference between these signals is calculated using the real function $A(\delta_x)$, the real constant B, and the complex function $C(\delta_x)$ derived in Appendix B. From (A10), the minimum $\alpha_{n\,\text{MIN}}(\delta_x)$ of (6) is given by

$$\alpha_{n\,\text{MIN}}(\delta_x) = \frac{A(\delta_x) - \dfrac{|C(\delta_x)|^2}{B}}{\dfrac{A(\delta_x) + B}{2}}. \tag{10}$$

For the case $n_0 + \delta_x < 0$, by substituting (B2), (B4), and (B6) in Appendix B into (10)

$$\alpha_{n\,\text{MIN}}(\delta_x) = \frac{2[1 - |z_0|^{2(N+n_0+\delta_x)}][1 - |z_0|^{-2(n_0+\delta_x)}]}{(1 - |z_0|^{2N})[2 - |z_0|^{2N} - |z_0|^{2(N+n_0+\delta_x)}]}. \tag{11}$$

For the case $n_0 + \delta_x \geq 0$, by substituting (B3), (B4), and (B7) into (10)

$$\alpha_{n\,\text{MIN}}(\delta_x) = 0. \tag{12}$$

The characteristics of the minimum $\alpha_{n\,\text{MIN}}(\delta_x)$ of (11) and (12) are shown in Fig. 3(a). For the case $n_0 + \delta_x < 0$, by setting $\beta_n(\delta_x)$ in (4) by $z_0^{-n_0-\delta_x}$, $\alpha_{n\,\text{MIN}}(\delta_x)$ is always zero. Thus, it is difficult to uniquely determine the true value $-n_0$ of δ_x from the curve of $\alpha_{n\,\text{MIN}}(\delta_x)$ obtained by the standard complex correlation approach.
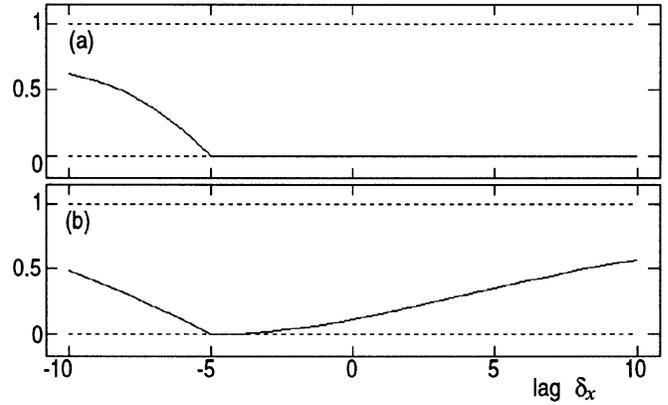

Fig. 3. (a) The characteristics of the minimum $\alpha_{n\,\text{MIN}}(\delta_x)$ of (11) and (12), which are derived from the standard normalized mean squared difference between the signals in Fig. 2(a) and (b). For the case $\delta_x \geq -n_0 = -5$, $\alpha_{n\,\text{MIN}}(\delta_x)$ is zero. Thus, it is impossible to uniquely determine the true value $-n_0$ of δ_x from $\alpha_{n\,\text{MIN}}(\delta_x)$. (b) The characteristics of the minimum $\alpha_{\text{MIN}}(\delta_x)$ of (19) and (20), which are derived by introducing the restriction into the normalized mean squared difference between the signals in Fig. 2(a) and (b). The $\alpha_{\text{MIN}}(\delta_x)$ takes the minimum only at the true lag of -5. Thus, the introduction of the restriction is effective in determination of lag between these complex signals.

C. Tracking Object Position Using the Constraint Least-Squares Method

As described above for the simple example, the waveform of $y(x; t + \Delta T)$ fits well with $y(x; t)$ for many candidates of δ_x if the fitness is evaluated by the normalized mean squared difference defined in (4). To solve the above problem, let us introduce the constraint least-squares method [31] by which the phase change rather than the magnitude change between these signals is evaluated. Let us redefine the normalized mean squared difference of (4) between the demodulated complex signal $y(x + \delta_x; t + \Delta T)$ and the preceding signal $y(x; t)$ by $\alpha(\beta; \delta_x)$

$$\alpha(\beta; \delta_x) = \frac{\displaystyle\sum_{x \in R} |y(x + \delta_x; t + \Delta T) - \beta(\delta_x)y(x; t)|^2}{\dfrac{\displaystyle\sum_{x \in R}\{|y(x + \delta_x; t + \Delta T)|^2 + |y(x; t)|^2\}}{2}} \\ - \gamma[|\beta(\delta_x)|^2 - 1] \tag{13}$$

where $\beta(\delta_x)$ is the phase change from $y(x; t)$ to $y(x+\delta_x; t+\Delta T)$. The magnitude of $\beta(\delta_x)$ is restricted to be one. This restriction is realized by introducing the Lagrange multiplier γ into the second term in the right-hand side of (13). As described in Appendix C, the minimization of $\alpha(\beta; \delta_x)$ under the restriction $|\beta(\delta_x)|^2 = 1$ is achieved by

$$\hat{\beta}(\delta_x) = \frac{\displaystyle\sum_{x \in R} y^*(x; t) \cdot y(x + \delta_x; t + \Delta T)}{\left|\displaystyle\sum_{x \in R} y^*(x; t) \cdot y(x + \delta_x; t + \Delta T)\right|}. \tag{14}$$

See (C15) in Appendix C. For this value of $\hat{\beta}(\delta_x)$, the minimum $\alpha_{\mathrm{MIN}}(\delta_x)$ is given by

$$\alpha_{\mathrm{MIN}}(\delta_x) \stackrel{\mathrm{def}}{=} \min_{\beta} \alpha_{\mathrm{MIN}}(\beta; \delta_x)$$

$$= 1 - \frac{\left| \sum_{x \in R} y^*(x; t) \cdot y(x + \delta_x; t + \Delta T) \right|}{\dfrac{\sum_{x \in R} \{ |y(x; t)|^2 + |y(x + \delta_x; t + \Delta T)|^2 \}}{2}}$$

(15)

from (C17) in Appendix C. By introducing the restriction, a solution quite different from (6) of the nonrestricted definition in (4) is obtained. The second term of (15) corresponds to the magnitude of the normalized cross-correlation function between $y(x; t)$ and $y(x; t + \Delta T)$.

Let us denote $\hat{\delta}_x$, by which $\alpha_{\mathrm{MIN}}(\hat{\delta}_x) = \alpha(\hat{\beta}; \hat{\delta}_x)$ takes the minimum, that is

$$\min_{\delta_x} \alpha_{\mathrm{MIN}}(\delta_x) = \alpha_{\mathrm{MIN}}(\hat{\delta}_x)$$
$$= \alpha(\hat{\beta}; \hat{\delta}_x). \quad (16)$$

For this $\hat{\delta}_x$, the phase change $\hat{\beta}(\hat{\delta}_x)$ during the period ΔT is determined and the average velocity in (3) is given by

$$\hat{v}\left(x; t + \frac{\Delta T}{2}\right) = c_0 \cdot \frac{\angle \hat{\beta}(\hat{\delta}_x)}{2\omega_0 \cdot \Delta T} \quad (17)$$

where $\angle \hat{\beta}(\hat{\delta}_x)$ denotes the phase value in the radian of $\hat{\beta}(\hat{\delta}_x)$. By multiplying the resultant velocity $\hat{v}(x; t + \Delta T/2)$ by the period ΔT, the next object position $\hat{x}(t)$ is estimated by

$$\hat{x}(t) = \hat{x}(t - \Delta T) + \hat{v}\left(x; t + \frac{\Delta T}{2}\right) \cdot \Delta T. \quad (18)$$

From the resultant object position $\hat{x}(t)$ and the velocity $\hat{v}(x; t + \Delta T/2)$, the object position and the vibration velocity on a large amplitude *motion* are simultaneously determined.

For the simple model described in (7) and (8), the minimum $\alpha_{\mathrm{MIN}}(\delta_x)$ is calculated as follows. By substituting $A(\delta_x)$, B, and $C(\delta_x)$ obtained in (B2)–(B6) of Appendix B into $\alpha_{n\,\mathrm{MIN}}(\delta_x) = 1 - 2|C(\delta_x)|/[A(\delta_x) + B]$ of (C16) in Appendix C, for the case $n_0 + \delta_x < 0$

$$\alpha_{\mathrm{MIN}}(\delta_x) =$$
$$\frac{1 - |z_0|^{2N} + [1 - 2|z_0|^{-(n_0 + \delta_x)}][1 - |z_0|^{2(N + n_0 + \delta_x)}]}{1 - |z_0|^2}$$

(19)

and for the case $n_0 + \delta_x \geq 0$

$$\alpha_{\mathrm{MIN}}(\delta_x) = \frac{[1 - |z_0|^{(n_0 + \delta_x)}]^2}{1 + |z_0|^{2(n_0 + \delta_x)}}. \quad (20)$$

The characteristics of the minimum $\alpha_{\mathrm{MIN}}(\delta_x)$ of (19) and (20) are shown in Fig. 3(b). As shown in this curve, $\alpha_{\mathrm{MIN}}(\delta_x)$ takes the minimum only at the true lag of -5. Thus, by introducing the restriction into the cost function into (13),

the lag between the successively received complex signals is uniquely determined.

The demodulated signal is A/D converted at a sampling interval of T_s. Nevertheless, the resultant estimate $\hat{x}(t)$ of the next object position in (18) is represented not by a discrete value, but by the continuous value in the above procedure because the instantaneous velocity $v(x; t)$ is given from the phase difference $\Delta\theta(x; t)$ in (3). When the velocity is assumed to be 5 mm/s, for example, and the time interval ΔT of the transmission of the RF pulses is $200\,\mu\mathrm{s}$, the displacement $\Delta x(t) = x(t + \Delta t) - x(t)$ of the object is $1\,\mu\mathrm{m}$ during the time interval ΔT, which is much less than the spatial resolution $\Delta x_S = T_S \times c_0/2 = 750\,\mu\mathrm{m}$ of Fig. 1 in the depth direction when the sampling period T_S is $1\,\mu\mathrm{s}$. Even if the sampling period T_s of 100 ns is employed, the resultant spatial resolution $\Delta x = 75\,\mu\mathrm{m}$ is still larger than the displacement of $1\,\mu\mathrm{m}$. Thus, an accurate tracking of the object is realized by this method.

If the maximum value of the velocity is 0.1 m/s, the displacement $\Delta x(t)$ of the object during the time interval ΔT is $20\,\mu\mathrm{m}$, which is comparable with the spatial resolution of $\Delta x_S = 75\,\mu\mathrm{m}$ in the depth direction when the sampling period of $T_S = 100$ ns is employed. If the object position is on the boundary of the sampling interval of Δx_S, this displacement is not negligible and the possible values of δ_x are -1, 0, and $+1$ for this case. For the case of $T_S = 1$ μs, however, the spatial resolution Δx_S is $750\,\mu\mathrm{m}$ and the above-mentioned displacement of the object is neglected. For this case, the proposed method does not differ from the conventional complex autocorrelation procedure except for the recursive adjustment of the sample window position based on the displacement estimated by integration of the instantaneous velocity.

D. Theoretical Comparison Between the Proposed Method and the PLL-Based Method

In our method, by applying the constraint least-square method to the demodulated reflected signal $y(x; t + \Delta T)$ and the preceding signal $y(x; t)$, the *motion* of the object is accurately tracked from the phase $\angle \hat{\beta}(\hat{\delta}_x)$ at the peak position $\hat{\delta}_x$ of the resultant complex correlation functions.

The proposed method differs from previous tracking methods in the following ways. In the standard cross-correlation-based method, as described in [11], it is well known that the velocity of the blood flow is obtained from the cross correlation if the blood vessel is at rest, that is, if the position of the region of interest is unchanged. For the problem described in this paper, however, there is a *motion* with large amplitude and the next object position is estimated from the displacement of the object by multiplying the resultant velocity by the time interval ΔT of the transmitted pulses. Thus, the spatial resolution in the estimation of the object displacement is achieved in less than several micrometers in this paper, which corresponds to the cases where the reflected signal is A/D converted with a sampling period of less than several ns ($= 2\times$ several micrometers/sound speed), which cannot be realized at present by the digitization of the data because a huge scaled
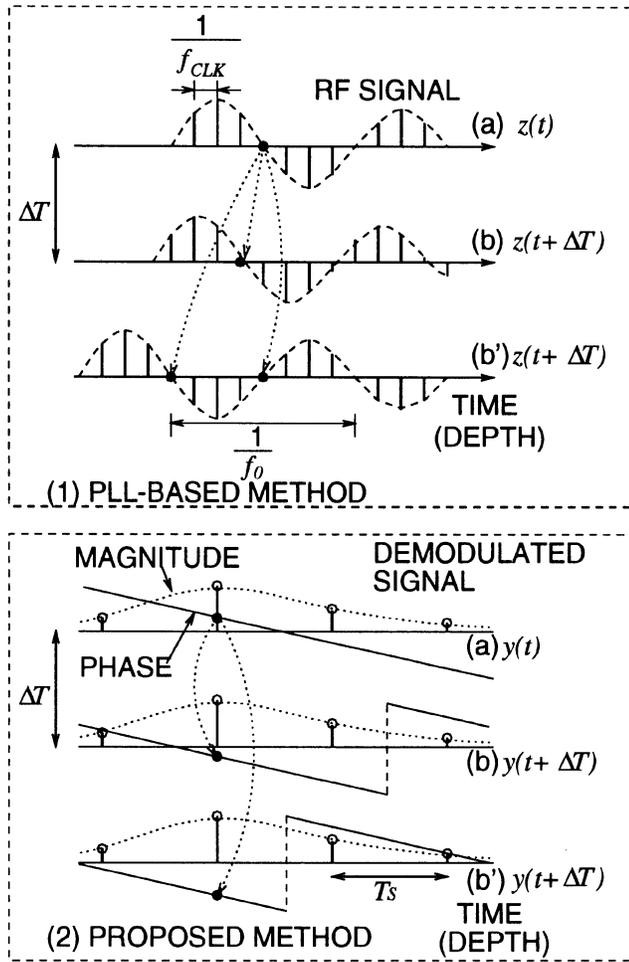
Fig. 4. An illustration explaining theoretical limitations in the estimation of the velocity of an object by 1) the previous PLL-based method and 2) the method proposed in this paper: (a) for the signal at a time t, (b) an example of the succeeding signal at a time $t + \Delta T$, and (b') another example of the succeeding signal at a time $t + \Delta T$.

memory is necessary for continuous digitization for periods of several heartbeats.

As shown in Fig. 4(2), based on the sampling theorem, the absolute magnitude of the phase difference during the time interval ΔT must be less than π. Let us assume that the magnitude and the phase of the complex signal $y(x; t)$ is represented by Fig. 4(2)(a) at a time t. At the next time, $t + \Delta T$ of the case in Fig. 4(2)(b), the velocity is correctly determined, while for the case Fig. 4(2)(b') the phase difference $\theta(t + \Delta T) - \theta(t)$ is equal to π, which corresponds to the upper limit. From (17), this condition determines the upper limit $|\hat{v}_{\max}|$ in the velocity estimation as follows:

$$|\hat{v}_{\max}| \leq \frac{c_0 \pi}{2\omega_0 \Delta T} = \frac{c_0}{4 f_0 \Delta T}. \tag{21}$$

Fig. 5 explains the relationship between the true velocity and the velocity estimates. The upper limit $|\hat{v}_{\max}|$ of (21) is shown by the upper horizontal line in Fig. 5. For the case where the absolute value of the velocity is less than the upper limit $|\hat{v}_{\max}|$, the velocity is correctly estimated by the proposed method as shown by the broken line in the same figure.
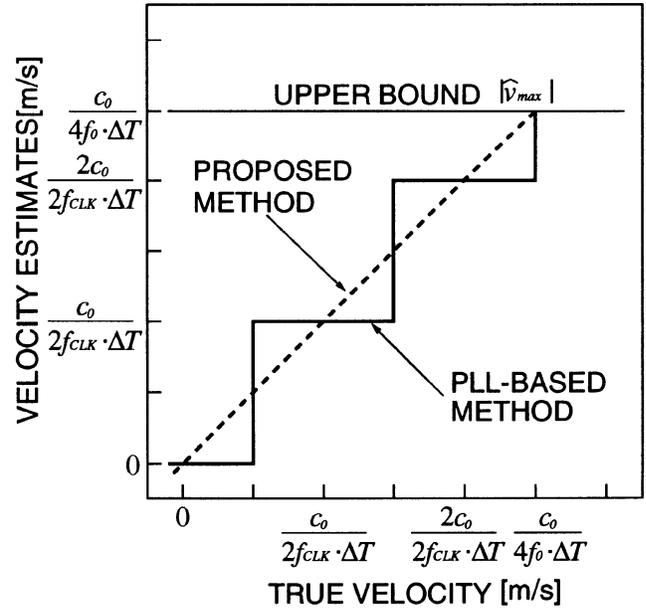

Fig. 5. Theoretical comparison of error and the limitation $|\hat{v}_{\max}|$ in the estimation of the velocity of an object by the previous PLL-based method and the method proposed in this paper. The upper limit $|\hat{v}_{\max}|$ of (21) and (22) is shown by the upper horizontal line. For the case where the absolute value of the velocity is less than the upper limit $|\hat{v}_{\max}|$, the velocity is correctly estimated by the proposed method as shown by the broken line. In the PLL-based method, however, the object displacement during the time interval ΔT is digitalized at a time interval $1/f_{CLK}$, that is, the spatial resolution is $1/f_{CLK} \times c_0/2$ in the depth direction, as shown by the solid line. There is a quantization error which is not negligible.

On the other hand, let us consider the upper limit in the previous PLL-based method. In the PLL-based method, the zero-cross timing of the successively received RF signal $z(t + \Delta T)$ is searched for around the position which was determined for the previously received RF data $z(t)$ by a digital circuit with the clock frequency f_{CLK} as shown in Fig. 4(1).

Thus, if the object displacement during the interval ΔT is more than $1/(2 f_0) \times c_0/2$ as shown in the relationship between Fig. 4(1)(a) and (1)(b'), the sampling theorem does not hold. Thus, the upper limit of this PLL-based method is described by

$$|\hat{v}_{\max}| \leq \frac{c_0}{2 f_0 \cdot 2} \times \frac{1}{\Delta T} = \frac{c_0}{4 f_0 \Delta T} \tag{22}$$

which of course coincides with that of (21). In the PLL-based method, however, the object displacement during the time interval ΔT is digitalized at a time interval $1/f_{CLK}$, that is, the spatial resolution is $1/f_{CLK} \times c_0/2$ in the depth direction, as shown by the solid line in Fig. 5. There is a quantization error.

For example when $\Delta T = 200$ μs, $f_0 = 4$ MHz, $c_0 = 1500$ m/s, $T_s = 1$ μs, and $f_{CLK} = 20$ MHz, the upper limit $|\hat{v}_{\max}|$ in (21) and (22) is equal to 0.469 m/s. The quantization error in the search for the zero-crossing point in the PLL-based method is equal to 0.188 m/s which is 40% that of $|\hat{v}_{\max}|$. This error is not negligible even for the case $f_{CLK} = 50$ MHz.

As described above for the PLL technique, the spatial resolution of the tracking is limited to the clock frequency (= several tens of megahertz) of the employed circuit. Thus,

the PLL technique cannot reach the spatial resolution obtained by the method proposed in this paper. The method proposed herein makes it possible to continuously transcutaneously measure the small vibration signals on a *motion* with a large amplitude resulting from the heartbeat in a wide frequency range.

III. A MEASUREMENT SYSTEM

In order to realize the procedure proposed in Section II-C, a high-speed A/D converter with a large-scale memory and a workstation are employed to analyze the complex signal, $y(t)$, resulting from the quadrature modulation of the signal $z(t)$ received by the sector-type ultrasonic transducer in the standard ultrasonic diagnostic equipment (Toshiba SSH-160A). In the diagnostic equipment, the standard B-mode cross-sectional image and M-mode image are displayed to identify the measurement points on the heart wall. The frequency f_0 of the transmitted ultrasound and repetition interval ΔT of the transmission of the ultrasonic pulses are employed as 3.75 MHz and 222 μs, respectively, in the experiments detailed in Sections IV, V, and VI.

The signal, $z(t)$, received by the ultrasonic transducer is amplified and demodulated by the ultrasonic diagnostic equipment. The resultant real signal, $y_r(t)$, and imaginary signal, $y_i(t)$, are simultaneously A/D converted with a two-channel 12-b A/D converter at a sampling rate of $1/T_S$. The sampling rate in the system is variable from 1 to 10 MHz, and herein 1 MHz is employed in the following experiments. In the A/D converter employed, the length of each signal is limited to 1 046 000 points ($\simeq$1 megawords). However, by digitizing the real and imaginary signals only for the period of length T_0 where the signal reflected at the object is received by the ultrasonic transducer, the effective length of the digital signal in the A/D converter is increased from one second to several seconds ($=$ several beat periods). For this intermittent digitization, the sampling clock of 1 MHz is generalized only for the period T_0 by an external signal generator, which is completely synchronous with the master clock of the ultrasonic diagnostic equipment. The demodulated clock is also synchronous with the master clock.

Then, by applying the proposed method described in Section II-C to the resultant digital signals, the velocity signal, denoted by $\hat{v}_{us}(t)$, is obtained at the workstation, which is connected with the A/D converter via a GPIB interface. The electrocardiogram (ECG) and phonocardiogram (PCG) are also digitized so that their timing is synchronous with that of the ultrasonic wave transmission from the transducer. The total time from the beginning of the A/D conversion to the display of the waveform on the display is several minutes.

IV. VALIDATION EXPERIMENTS USING A WATER TANK

To confirm the principle of the proposed method, a small vibration signal $v(t)$ of a rubber plate in a water tank as shown in Fig. 6 is estimated from the signal received by an ultrasonic transducer. A *motion* with a large amplitude ($\pm$7.5 mm, 1 Hz), which corresponds to heartbeat, is generated by the rotation of an eccentric cam. A vibration with a small
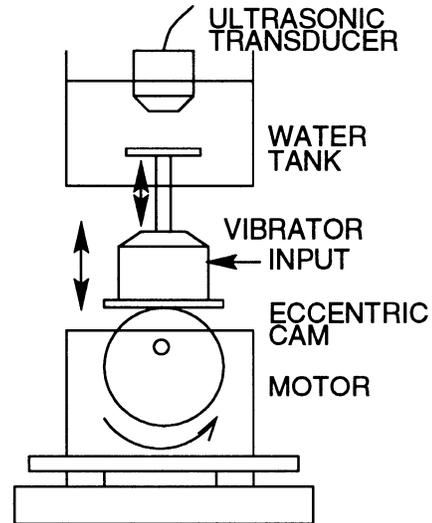

Fig. 6. An experimental system which simulates the vibration on the ventricle wall with a heartbeat of large amplitude using a vibrator and a motor with an eccentric cam. The motor with the eccentric cam generates motion having a large amplitude of ±7.5 mm and a frequency of 1 Hz which corresponds to a heartbeat. The vibrator imposes a small amplitude vibration ranging from 30 to 1000 Hz with amplitude of 20 μm peak to peak on this motion.

amplitude, which corresponds to the vibration on the wall of a ventricle, is generated by a vibrator (Brüel & Kjær, 4810) on the eccentric cam. In this experiment, the vibrator is excited by band-limited noise ranging from 30 to 1000 Hz with an amplitude of 5 V_{p-p}. The vibrator generates displacement of the rubber plate which corresponds to the input voltage signal. The amplitude of the corresponding displacement due to the vibrator is about 20 μm peak to peak.

Fig. 7(a)–(c) shows the standard B-mode cross-sectional image, the velocity, and M-mode images, respectively, which are obtained by the standard ultrasonic diagnostic equipment. As found in Fig. 7(b), the velocity of the rubber object cannot be obtained for the whole period, since the measured point is fixed in space and the length of the sample volume is shorter than the amplitude of the *motion* due to the eccentric cam. The motion with large amplitude is shown in the M-mode image of Fig. 7(c), however, the waveform of the small vibration due to the generator cannot be recognized. One of the purposes of this paper is to measure the small vibration signal, which should be within the thickness of the curved line due to the motion of Fig. 7(c) in the M-mode image.

By applying the proposed method in Section II-C to the digital signals in the measurement system described in Section III, the velocity signal, denoted by $\hat{v}_{us}(t)$, is obtained. The input voltage signal $V_{in}(t)$ of the vibrator and the output signal $v_{laser}(t)$ of a laser Doppler velocimeter (Ono Sokki LV1300, Hakusan 1-16-1, Midori-ku, Yokohama, Japan) are also A/D converted simultaneously.

Fig. 8 shows the results of these experiments. Fig. 8(b) shows the input signals $V_{in}(t)$ of the vibrator. Fig. 8(a) shows the estimates of the object *motion* $\hat{x}_A(t)$ obtained by the proposed method in (18), which is superimposed on the M-mode image generated from the magnitude of the demodulated received signal $y(x; t)$. In these experiments, since the length of the transmitted RF signal is about 3 μs, the range R
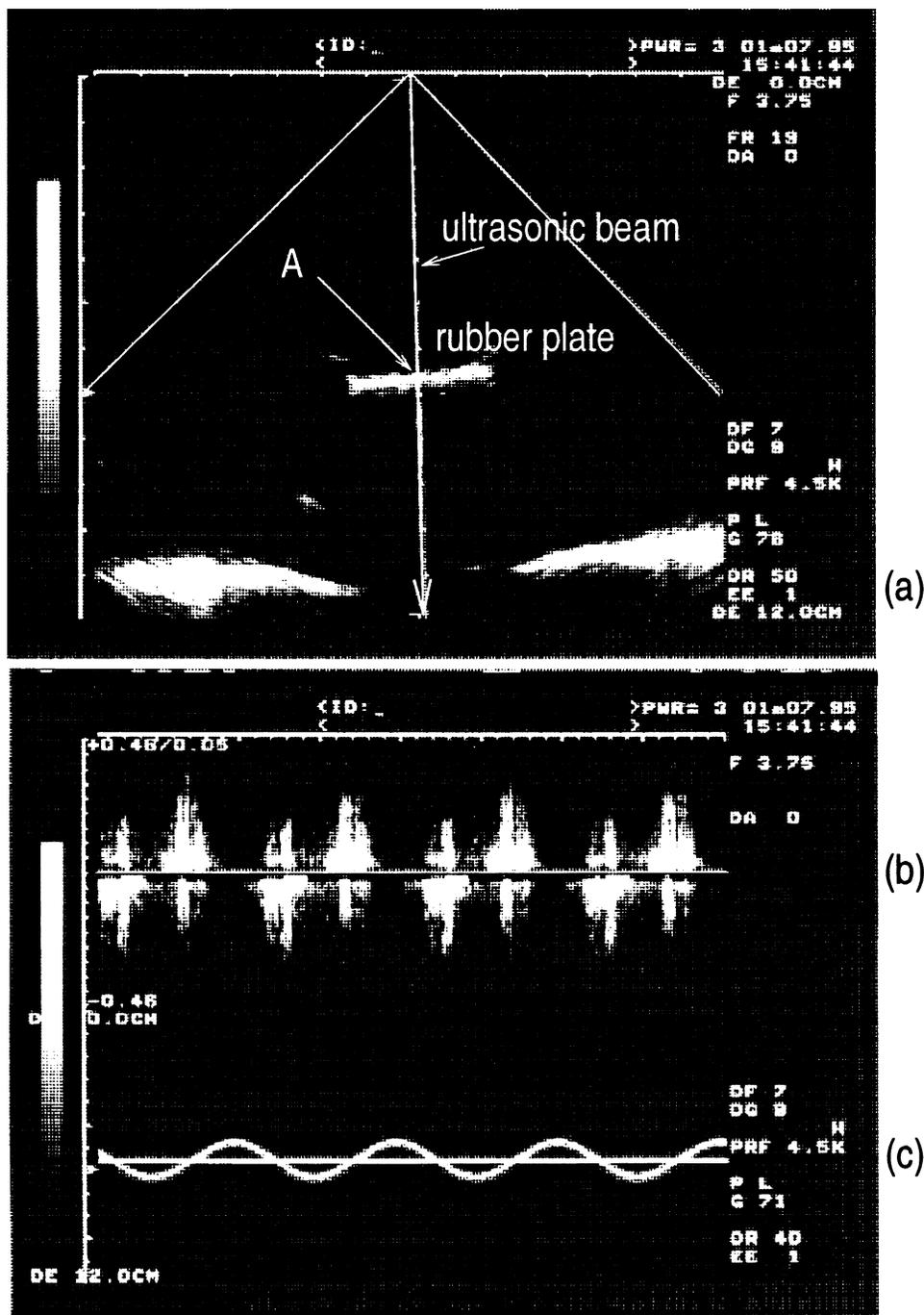
Fig. 7. Results obtained by standard ultrasonic equipment in the experiments on the detection of the vibration signals on the rubber plate of the vibrator on the eccentric cam in the water tank of Fig. 6. (a) B-mode image showing the cross-sectional image around measured point A. The scale of the vertical and that of the horizontal axes are 1 cm, and (b) the velocity measured at a fixed position of the sample volume, which is indicated at point A in (a). The scales of the vertical axis and the horizontal axis are 0.05 m/s and 100 ms, respectively, and (c) the M-mode image showing the slow motion on the axis across point A. The scale of the vertical axis is 1 cm in depth.

employed in the calculating correlation function in (13) is ± 1 point in length. The tracking result $\hat{x}_A(t)$ of point A exactly coincides with the M-mode image as shown in Fig. 8(a).

Fig. 8(d) shows the vibration velocity signal $\hat{v}_{us}(t)$ estimated by the proposed method in (17). The amplitude of the signal $\hat{v}_{us}(t)$ in Fig. 8(d) is similar to that of the signals $v_{laser}(t)$ obtained by laser Doppler velocimeter in Fig. 8(c). A high-pass filter with a cutoff frequency of 0.5 Hz is employed

in the laser Doppler velocimeter. Due to this filter, it is experimentally found that there is a time delay of about 850 ms only for the low-frequency component of 1 Hz generated by the rotation of the eccentric cam. By considering the time delay, these waveforms of $\hat{v}_{us}(t)$ and $v_{laser}(t)$ almost completely coincide in the *low*-frequency components.

To compare the *high*-frequency components of these signals, Fig. 9(a)–(c) shows the waveforms of the input voltage signal
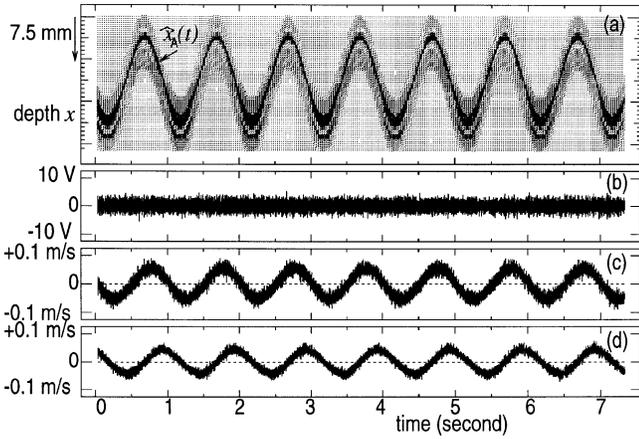
Fig. 8. Estimation results using the experimental system shown in Fig. 6: (a) the object motion $\hat{x}(t)$ estimated by the proposed method, superimposed on the M-mode image, obtained by the magnitude of the received signal, (b) input voltage signal $V_{input}(t)$ of the vibrator by which a vibration of band-limited noise ranging from 30 to 1000 Hz with an amplitude of 20 μm peak to peak is generated, (c) the velocity signal $v_{laser}(t)$ obtained by laser Doppler velocimeter, and (d) the vibration velocity signal $\hat{v}_{us}(t)$ estimated by the proposed method.
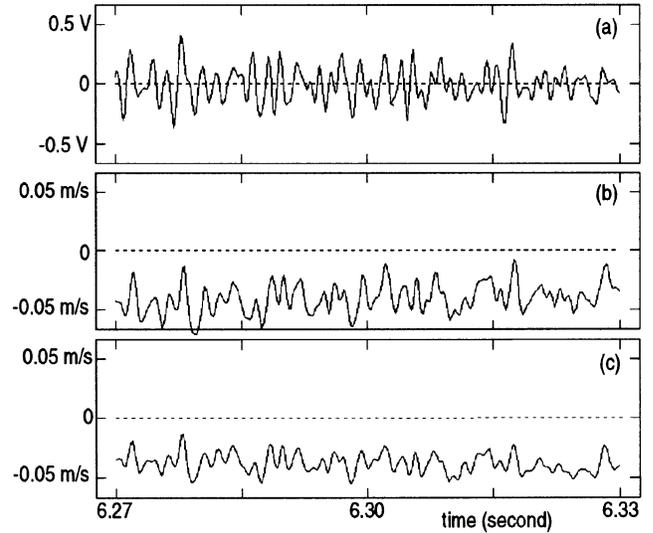

Fig. 9. To compare the high-frequency components of the waveforms in Fig. 8, (a)–(c) show the waveforms of the input voltage signal $V_{in}(t)$ of the vibrator, the output signal $v_{laser}(t)$ of a laser Doppler velocimeter, and the vibration velocity signal $\hat{v}_{us}(t)$ estimated by the proposed method, respectively, during the period from 6.27 to 6.33 s in Fig. 8.

$V_{in}(t)$ of the vibrator, the output signal $v_{laser}(t)$ of a laser Doppler velocimeter, and the vibration velocity signal $\hat{v}_{us}(t)$ estimated by the proposed method, respectively, during the period from 6.27 to 6.33 s in Fig. 8. Though there is a slight difference in amplitude of these signals, their waveforms are similar. The result in Fig. 9(b) obtained by the laser Doppler is correct as to amplitude. In the proposed procedure using the ultrasonic Doppler, however, the instantaneous velocity $v(t)$ is obtained from (3) by assuming that there is only one frequency component with a center frequency component of $f_0 = \omega_0/2\pi$ in the employed ultrasonic wave. However, the pulsive ultrasonic wave has a frequency band of about 1 MHz around the center frequency. At the same time, there is larger attenuation for the higher frequency components of the ultrasonic wave. Thus, the velocity in Fig. 9(c) obtained by the ultrasonic Doppler-based method is slightly underestimated.

To quantitatively evaluate the correlation at each frequency f among the estimated signal $\hat{v}_{us}(t)$ in Fig. 8(d), $v_{laser}(t)$ in Fig. 8(c), and $V_{in}(t)$ in Fig. 8(b), the following squared magnitudes of coherence functions $|\gamma_{in \leftrightarrow us}(f)|^2$ and $|\gamma_{laser \leftrightarrow us}(f)|^2$ are evaluated:

$$|\gamma_{in \leftrightarrow us}(f)|^2 = \frac{|E[V_{in}(f)^* \cdot \hat{V}_{us}(f)]|^2}{E[|V_{in}(f)|^2] \cdot E[|\hat{V}_{us}(f)|^2]} \quad (23)$$

$$|\gamma_{laser \leftrightarrow us}(f)|^2 = \frac{|E[V_{laser}(f)^* \cdot \hat{V}_{us}(f)]|^2}{E[|V_{laser}(f)|^2] \cdot E[|\hat{V}_{us}(f)|^2]} \quad (24)$$

where $\hat{V}_{us}(f)$, $V_{in}(f)$, and $V_{laser}(f)$ are the spectra of $\hat{v}_{us}(t)$, $V_{in}(t)$, and $v_{laser}(t)$, respectively. The term $E[\cdot]$ denotes the average operation. There are 27 averaging operations in this experiment. The squared magnitude of coherence function quantitatively evaluates the correlation between the two signals for each frequency component [33]. If the squared magnitude of coherence function, $|\gamma(f)|^2$, between two signals is equal to one, there is complete correlation between these signals for the frequency component f. That is, one signal is completely
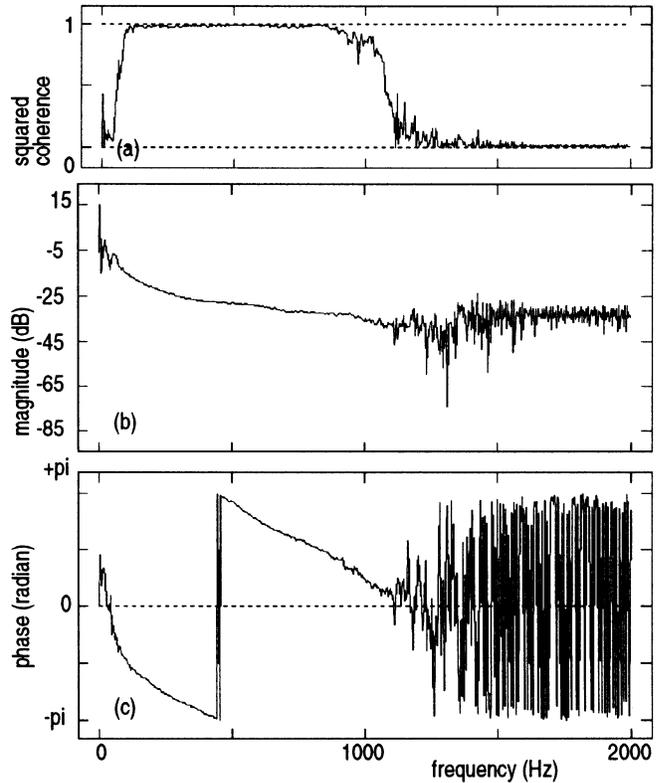

Fig. 10. (a) The squared magnitude of coherence function $|\gamma_{in \rightarrow us}(f)|^2$ between $V_{in}(t)$ and $\hat{v}_{us}(t)$, (b) the magnitude of the transfer function $H_{in \rightarrow us}(f)$ from the input signal $V_{in}(t)$ to $\hat{v}_{us}(t)$ estimated by the proposed method in the frequency range up to near the Nyquist frequency $1/\Delta T$, and (c) the phase characteristics of the transfer function $H_{in \rightarrow us}(f)$.

described by the other signal and the linear relationship between them.

At the same time, the transfer function $H_{in \rightarrow us}(f)$ from $V_{in}(t)$ to $\hat{v}_{us}(t)$ and the transfer function $H_{laser \rightarrow us}(f)$ from
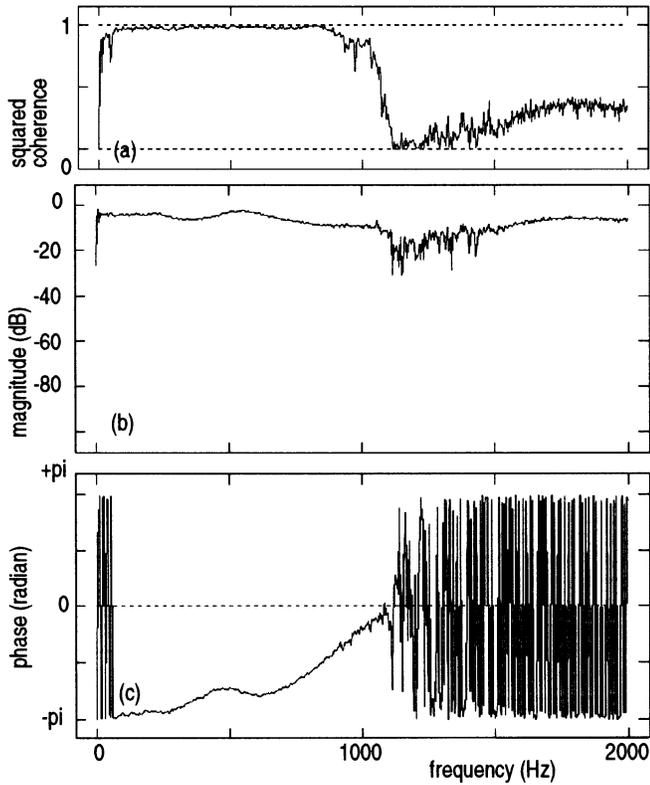
Fig. 11.   (a) The squared magnitude of coherence function $|\gamma_{laser \to us}(f)|^2$ between $v_{laser}(t)$ and $\hat{v}_{us}(t)$, (b) the magnitude of the transfer function $H_{laser \to us}(f)$ from $v_{laser}(t)$ to $\hat{v}_{us}(t)$ estimated by the proposed method, and (c) the phase characteristics of the transfer function $H_{laser \to us}(f)$.

Fig. 12.   The average values $\Gamma_{in \to us}$ and $\Gamma_{laser \to us}$ of the squared magnitude of coherence functions $|\gamma_{in \to us}(f)|^2$ and $|\gamma_{laser \to us}(f)|^2$, respectively, for various values of Δx of the range $R = [x(t) - \Delta x,\ x(t) + \Delta x]$ employed in (13). (a) The average values from the frequency ranges from 1 Hz to 1 kHz and (b) the average values from the frequency ranges from 900 Hz to 1 kHz. The optimum value of Δx is ± 1 point in length, that is, the range R corresponds to about ± 0.75 mm around the previously determined object position $x(t)$.

$v_{laser}(t)$ to $\hat{v}_{us}(t)$ are obtained as follows [33]:

$$H_{in \to us}(f) = \frac{E[V_{in}(f)^* \cdot \hat{V}_{us}(f)]}{E[|V_{in}(f)|^2]} \qquad (25)$$

$$H_{laser \to us}(f) = \frac{E[V_{laser}(f)^* \cdot \hat{V}_{us}(f)]}{E[|V_{laser}(f)|^2]}. \qquad (26)$$

Fig. 10(a)–(c), respectively, shows the resultant squared magnitude of coherence function $|\gamma_{in \leftrightarrow us}(f)|^2$ between $V_{in}(t)$, and $\hat{v}_{us}(t)$, and the magnitude and the phase of the transfer function $H_{in \to us}(f)$ from the input signal $V_{in}(t)$ to $\hat{v}_{us}(t)$ in the frequency range up to near the Nyquist frequency $1/2\Delta T$. Fig. 11(a)–(c), respectively, shows the resultant squared magnitude of coherence function $|\gamma_{laser \leftrightarrow us}(f)|^2$ between $v_{laser}(t)$ and $\hat{v}_{us}(t)$, and the magnitude and the phase of the transfer function $H_{laser \to us}(f)$ from $v_{laser}(t)$ to $\hat{v}_{us}(t)$.

From Figs. 10(a) and 11(a), the squared magnitude of coherence function is almost one from 30 Hz to 1 kHz. There are, therefore, linear relationships between $V_{in}(t)$ and $\hat{v}_{us}(t)$ and between $v_{laser}(t)$ and $\hat{v}_{us}(t)$. The input signal $V_{in}(t)$ does not include low-frequency components less than 30 Hz, while for $\hat{v}_{us}(t)$, the low-frequency components less than 100 Hz resulting from rotation of the eccentric cam are included. Thus, $|\gamma_{in \leftrightarrow us}(f)|^2$ in Fig. 10(a) is almost zero in the low-frequency range less than 100 Hz, in which low-frequency movements due to the eccentric cam are not negligible. However, since there are low-frequency components with large
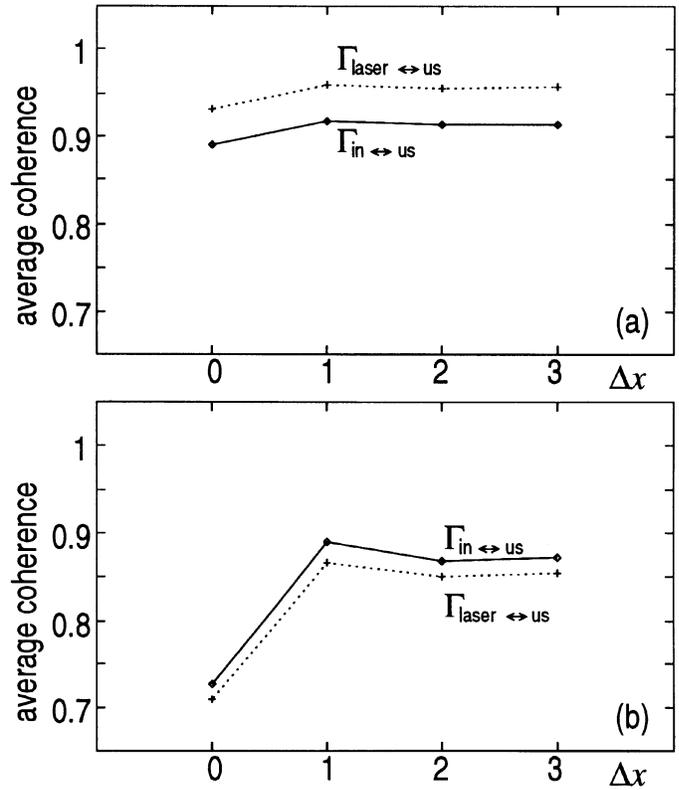
amplitude due to the eccentric cam in both $v_{laser}(t)$ and $\hat{v}_{us}(t)$, $|\gamma_{laser \leftrightarrow us}(f)|^2$ in Fig. 11(a) is almost one even in the low-frequency range.

From Fig. 10(c), the phase characteristics are described by an almost straight line in the frequency range from 100 Hz to 1 kHz. Though the phase characteristics $\angle H_{laser \to us}(f)$ in the low-frequency components of Fig. 11(c) are affected by the high-pass filter of 0.5 Hz employed in the laser Doppler velocimeter, the magnitude of the transfer function $H_{laser \to us}(f)$ of Fig. 11(b) is almost flat in the frequency range from 1 Hz to 1 kHz. There are differences from the optimum characteristics (flat magnitude and linear phase) of the transfer function. However, these differences can be corrected because the squared magnitude of coherence is almost one in the frequency range less than 1 kHz. From these experimental results, it is confirmed that the small vibration on the large *motion* is successfully detected by the proposed method in the frequency range from 1 to 1000 Hz.

Fig. 12 shows the average values, respectively denoted by $\Gamma_{in \leftrightarrow us}$ and $\Gamma_{laser \leftrightarrow us}$, of the squared magnitude of coherence functions $|\gamma_{in \leftrightarrow us}(f)|^2$ and $|\gamma_{laser \leftrightarrow us}(f)|^2$ for various values of Δx of the range $R = [x(t) - \Delta x,\ x(t) + \Delta x]$ employed in $\alpha(\beta; \delta_x)$ of (13). Fig. 12(a) and (b) shows the average values for the frequency ranges from 1 Hz to 1 kHz and from
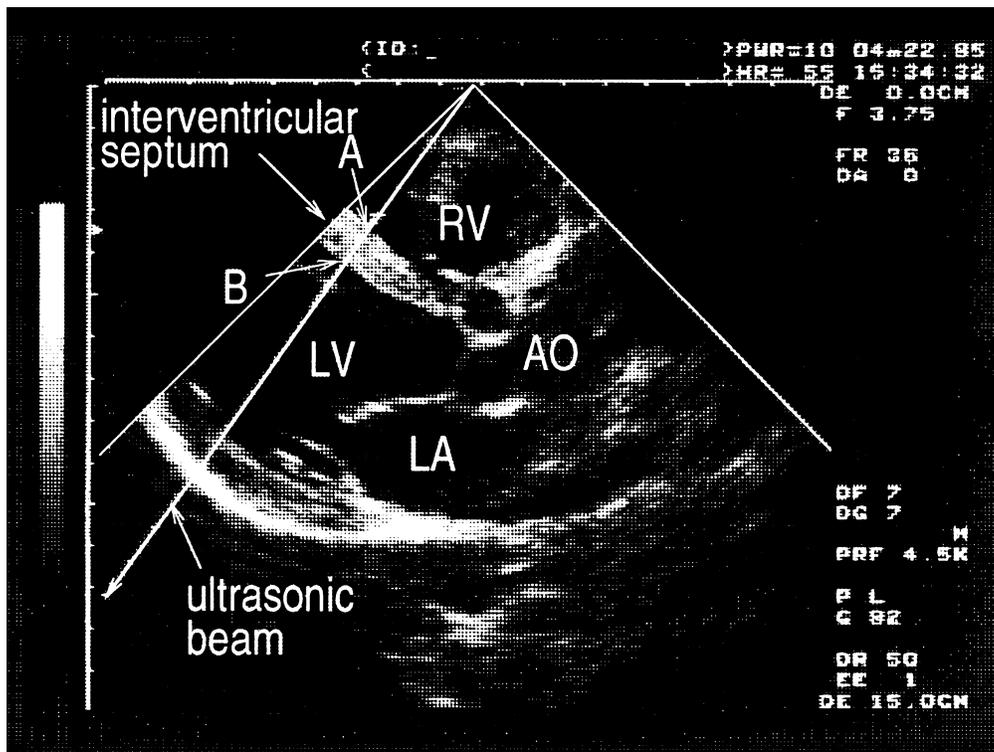
Fig. 13. A standard B-mode image showing the cross-sectional area around the two measured points, (A) and (B), in an *in vivo* experiment for the detection of vibrations on the interventricular septum of the left ventricle (LV) of a 23-year-old male patient with acute lymphoblastic leukemia who has been treated with antracenadiones. Points (A) and (B) are on the RV and LV surfaces of the interventricular septum, respectively. The ultrasonic beam passing through the two points is almost perpendicular to the septum during the measurements.

900 Hz to 1 kHz, respectively. For the frequency range from 900 Hz to 1 kHz in Fig. 12(b), the results vary remarkably. For the case of $\Delta x = 0$, the range R where the constraint cross-correlation function is evaluated has only one point and the velocity estimates are easily affected by additive noise. As range R increases, the effect of noise is decreased. At the same time, the spatial resolution is also decreased. From Fig. 12, it is found that the optimum value of Δx is ± 1 point in length, that is, range R corresponds to ± 0.75 mm around the previously determined object position $x(t)$. This value of $\Delta x = 1$ is employed in the following *in vivo* experiments.

V. *In Vivo* Detection of Heart Wall Vibrations

In order to noninvasively diagnose myocardial damage by adriamycin injection based on the acoustic characteristics of the myocardium, let us try to measure the small vibration signals on the heart wall from the precordium and apply spectrum analysis to the resultant vibration signals. It is, however, difficult to measure a small vibration signal with an amplitude less than 100 μm with the previously developed methods because such a small vibration is superimposed on the large *motion* resulting from a heartbeat with an amplitude of about ± 10 mm. For this problem, we apply the proposed method for noninvasive measurement of small vibration signals on the interventricular septum as follows.

First, the proposed method is applied to the detection of a vibration signal on the interventricular septum of a 23-year-old male patient with acute lymphoblastic leukemia who has been treated with antracenadiones. Fig. 13 shows the B-mode image around two measured points, (A) and (B). This image is obtained by standard ultrasonic diagnostic equipment. Points (A) and (B) are on the surface of the right ventricular (RV) side and the left ventricular (LV) side of the interventricular septum, respectively. The ultrasonic beam passing through points (A) and (B) is almost perpendicular to the interventricular septum as shown in Fig. 13.

Fig. 14(b) and (c) shows the ECG and the heart sound (PCG), respectively. The tracking results $\hat{x}_A(t)$ and $\hat{x}_B(t)$, estimated by (18) of the movement of points (A) and (B) are superimposed on the M-mode image in Fig. 14(a), which was obtained from the magnitude of the demodulated received signals. Fig. 14(d) and (e) shows the estimates of the vibration velocity signals $\hat{v}_A(t)$ and $\hat{v}_B(t)$ of the tracked points $\hat{x}_A(t)$ and $\hat{x}_B(t)$, respectively. The resultant vibration signals are sufficiently reproducible for the six heartbeat periods as shown in Fig. 14(d) and (e).

For the systolic phase, where the ventricular contraction begins near the peak of the R-wave of the ECG, the velocity estimates $\hat{v}_A(t)$ and $\hat{v}_B(t)$ of the septum have positive values after negative steep peaks as shown in Fig. 14(d) and (e); that is, the septum moves in the opposite direction of the ultrasonic transducer on the chest wall. The amplitude of $\hat{v}_B(t)$ on the LV side is a little greater than that of $\hat{v}_A(t)$ on the RV side, especially in the systolic phase. This is due to the thickness change of the interventricular septum.
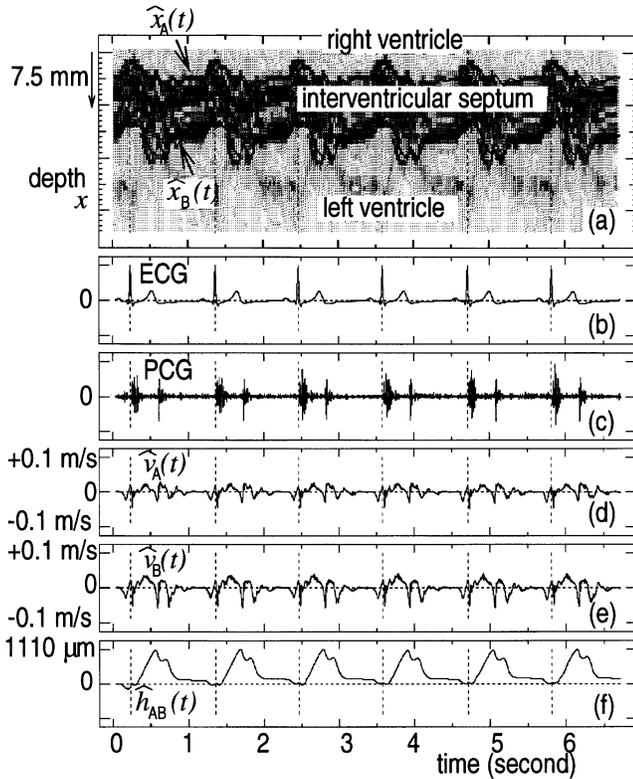
Fig. 14. *In vivo* experimental results of the vibration at points (A) and (B) on the RV and the LV surfaces of the interventricular septum, respectively, in Fig. 13: (a) the tracking results $\hat{x}_A(t)$ and $\hat{x}_B(t)$ in (18) of the points A and B. These results are superimposed on the M-mode image, (b) the ECG, (c) the PCG, (d), (e) the estimates of the vibration velocity signals $\hat{v}_A(t)$ and $\hat{v}_B(t)$ of points A and B, and (f) the change in thickness, $\hat{h}_{AB}(t)$, of the interventricular septum given by (27). The waveform of $\hat{h}_{AB}(t)$ is also reproducible for the six heartbeat periods.

Fig. 14(f) shows the thickness change, $\hat{h}_{AB}(t)$, of the interventricular septum from the thickness at the timing of the R-wave of ECG. $\hat{h}_{AB}(t)$ is given by

$$\hat{h}_{AB}(t) = \int \{\hat{v}_B(t) - \hat{v}_A(t)\} \, dt. \tag{27}$$

The waveform of $\hat{h}_{AB}(t)$ is also reproducible for the six heartbeat periods. For the systolic phase, the interventricular septum becomes about 1 mm thicker than that of the diastolic phase.

The waveforms of ECG, PCG, $\hat{v}_A(t)$, and $\hat{v}_B(t)$ of Fig. 14 from a P-wave to the next P-wave in the succeeding heartbeat are separated. The results for the first five heartbeats in Fig. 15 are overlaid and shown in Fig. 14. From Fig. 15(c) and (d), the reproducibility of $\hat{v}_A(t)$ and $\hat{v}_B(t)$ is *qualitatively* confirmed at least for the low-frequency components less than 20 Hz with large amplitude resulting from the heartbeat.

To *quantitatively* evaluate the reproducibility of the similarity of the M signals $\{u_i(t)\}$, $(i = 1, 2, \cdots, M)$ for each frequency component of f, the following reproducibility function $|\hat{\gamma}_0(f)|^2$ is introduced by (D5) as described in
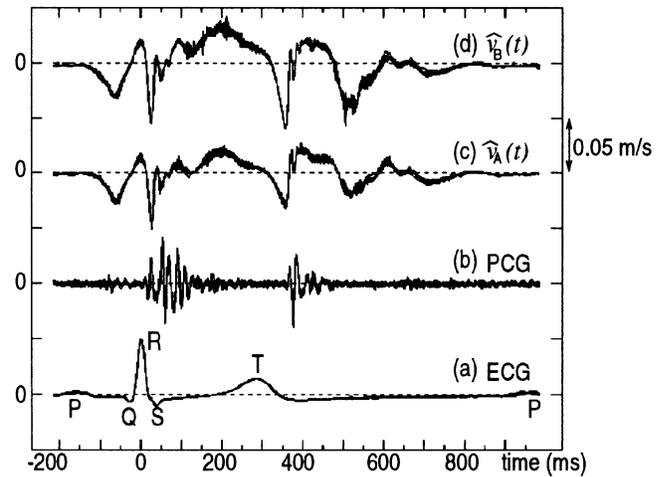

Fig. 15. The waveforms of ECG, PCG, $\hat{v}_A(t)$, and $\hat{v}_B(t)$ of Fig. 14 from a P-wave to the next P-wave in the succeeding heartbeat are separated. The results for the first five heartbeats in Fig. 14 are overlaid and shown: (a) the ECG, (b) the PCG, (c) and (d) the estimates of the vibration velocity signals $\hat{v}_A(t)$ and $\hat{v}_B(t)$ of points A and B. The reproducibility of $\hat{v}_A(t)$ and $\hat{v}_B(t)$ is qualitatively confirmed at least for the low-frequency components.

Appendix D:

$$|\hat{\gamma}_0(f)|^2 = \frac{\left|\sum_{i=1}^{M} U_i(f)\right|^2}{M \sum_{i=1}^{M} |U_i(f)|^2} \tag{28}$$

where $U_i(f)$ is the Fourier spectrum of $u_i(t)$. Similar to the squared magnitude of the coherence function, $|\hat{\gamma}_0(f)|^2$ also has a value from zero to one. If $|\hat{\gamma}_0(f)|^2$ is equal to one, M waveforms $\{u_i(t)\}$ completely coincide for the frequency component of f. If $|\hat{\gamma}_0(f)|^2$ is zero, there is no correlation among $\{u_i(t)\}$ for the frequency components of f.

The solid lines in Fig. 16(a) and (b) show the reproducibility function, $|\gamma_0(f)|^2$, evaluated for the components around the second heart sounds of the vibration signals $\hat{v}_A(t)$ and $\hat{v}_B(t)$ of the first five heartbeats in Fig. 14(d) and (e), respectively. Each spectrum is obtained by applying the fast Fourier transform (FFT) to $\hat{v}_A(t)$ and $\hat{v}_B(t)$ for the period of ± 100 ms around the second heart sound of each heartbeat. For these results, there is a high correlation between these small vibration signals for five heartbeats up to at least 100 Hz. Thus, the reproducibility of the measured vibrations is quantitatively confirmed.

The solid lines in Fig. 16(c) and (d) show the average power spectra of the signals $\hat{v}_A(t)$ and $\hat{v}_B(t)$ of the first five heartbeats in Fig. 14(d) and (e), respectively. The analyzed periods are same as those in Fig. 16(a) and (b). The minimum and maximum values of the power spectra of the vibration signals for five heartbeats are shown by the vertical bars for each frequency. As shown in these figures, there are large components in the low-frequency range less than 25 Hz, which correspond to the motion due to the heartbeats. However, there is enough reproducibility even for the high-frequency components from 25 to 90 Hz. The frequency component at 90 Hz is less than the maximum component at 10 Hz by
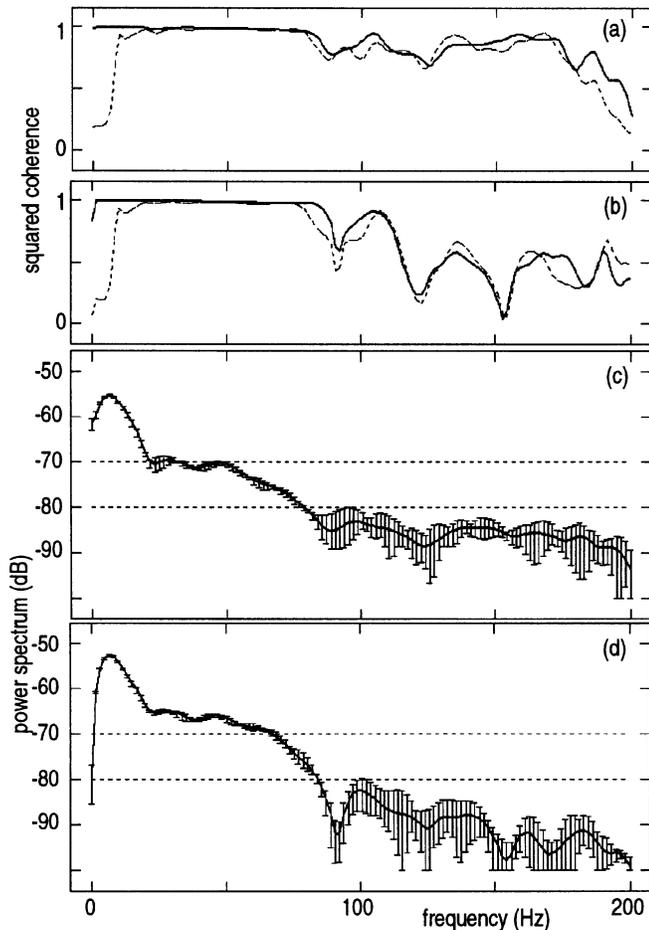
Fig. 16. (a) and (b) The solid lines show the reproducibility function, $|\gamma_0(f)|^2$, of the small vibration signals $\hat{v}_A(t)$ and $\hat{v}_B(t)$ for the first five heartbeats in Fig. 14(d) and (e), respectively. Each spectrum is obtained by applying FFT to $\hat{v}_A(t)$ and $\hat{v}_B(t)$ for the period of ± 100 ms around the second heart sound for each heartbeat, where the Hanning window is employed. There is a high correlation between these small vibration signals for five heartbeats up to at least 100 Hz. The broken lines show the squared magnitude of the standard coherence function between $\hat{v}_A(t)$ and PCG and between $\hat{v}_B(t)$ and PCG, respectively. The small vibration detected on the interventricular septum at the timing around the second heart sound has a high correlation with the second heart sound. (c) and (d) The average power spectra of $\hat{v}_A(t)$ and $\hat{v}_B(t)$, respectively. The analyzed periods are the same as those in (a) and (b). The vertical bar for each frequency shows the minimum and maximum values of the power spectra of the vibration signals.
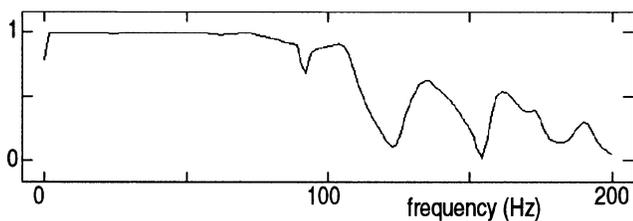

Fig. 17. The squared magnitude of the standard coherence function, $|\gamma_{AB}(f)|^2$, between $\hat{v}_A(t)$ of Fig. 14(d) and $\hat{v}_B(t)$ of Fig. 14(e) at the period ± 100 ms around the second heart sound. There is a correlation between these small vibration signals of both sides of the interventricular septum up to at least 100 Hz.

about 25 dB; that is, the amplitude of the components at 90 Hz is 1/20 that of the components at 10 Hz. For these small vibration components, which are within the thickness
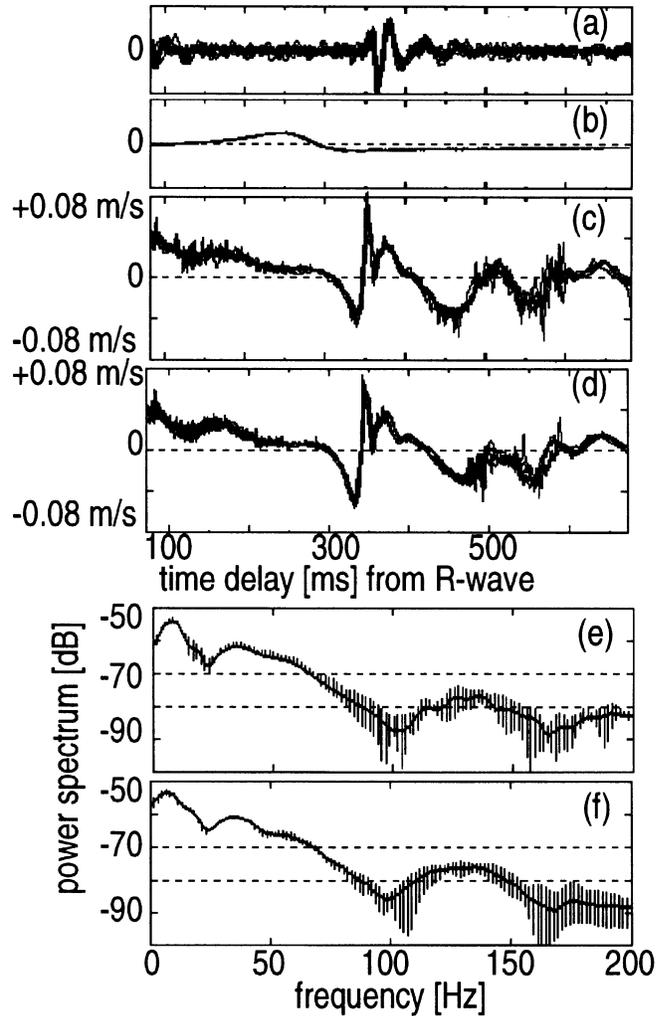

Fig. 18. (a) and (b) PCG and ECG measured when $\{v_B(t)\}$ of (c) are obtained. (c) and (d) The vibrations $\{v_B(t)\}$ at the LV side of the interventricular septum of a presumedly healthy 22-year-old male volunteer, where the measured point B is selected in the cross-sectional image along the longitudinal axis and the short axis, respectively, of the heart. The small vibration signals of six heartbeats are overlaid in each figure and the waveforms are shown for the period around the second heart sound. (e) and (f) Average power spectra of the signals in (c) and (d), respectively. The average power spectra of the vibration signals for six heartbeats are shown by the solid lines. The minimum and maximum values of the vibration signals for six heartbeats are shown by the vertical bars for each frequency component in the power spectra. The waveforms in (c) are similar to those in (d). The power spectrum in (e) is also similar to that in (f).

of the overlaid curves in Fig. 15(c) and (d), the waveform is accurately measured by the proposed method.

The broken lines in Fig. 16(a) and (b) show the squared magnitude of the standard coherence function between $\hat{v}_A(t)$ and PCG and between $\hat{v}_B(t)$ and PCG, respectively. It is known that the second heart sound is generated due to the closure of the aortic valve [34]. The small vibration on the interventricular septum measured here has a high correlation with the second heart sound, which is a clue for identifying the origin of the heart wall vibration detected here.

Fig. 17 shows the squared magnitude of the standard coherence function, $|\gamma_{AB}(f)|^2$, between $\hat{v}_A(t)$ and $\hat{v}_B(t)$ at the period ± 100 ms around the second heart sound. There is a
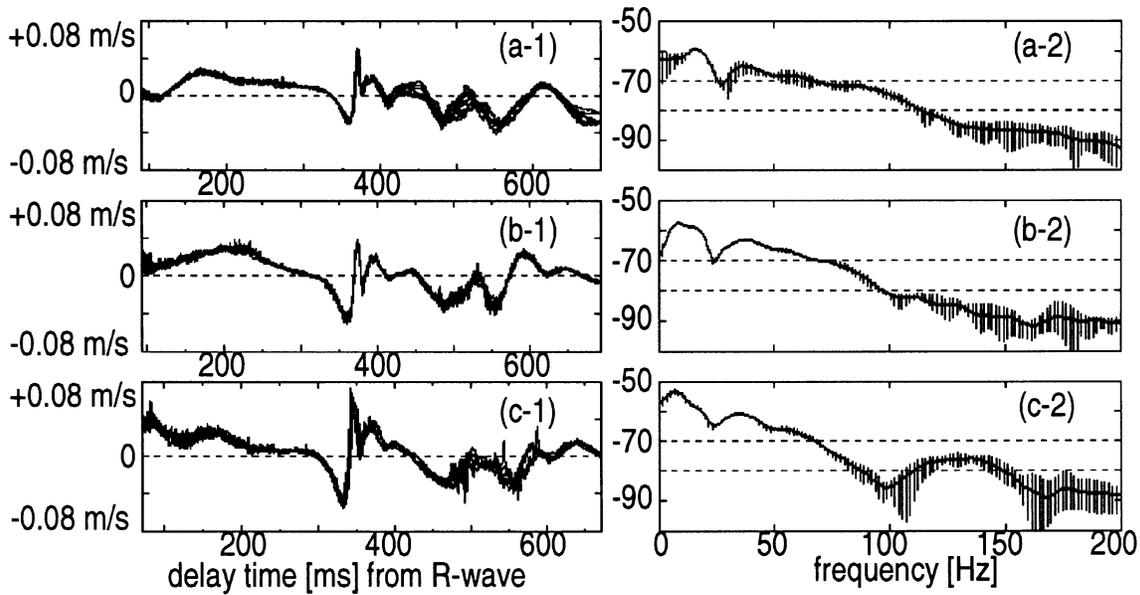
Fig. 19. The waveforms of the vibration signal on the LV side of the interventricular septum of three presumedly healthy young male volunteers and their average power spectra. (a) A presumedly healthy 22-year-old male volunteer; eight heartbeats overlaid, (b) a presumedly healthy 26-year-old male volunteer; five heartbeats overlaid, and (c) a presumedly healthy 22-year-old male volunteer; six heartbeats overlaid. The waveforms of the several heartbeats are overlaid and are shown at the moment of the second heart sound emission. For each subject, the reproducibility is quantitatively confirmed up to 100 Hz. For the power spectra, the employed liens are shown by a format similar to that in Fig. 18(e) and (f). The waveforms and power spectra of these volunteers are similar.

correlation up to at least 100 Hz between these small vibration signals on both sides of the interventricular septum.

As shown in Fig. 13, measured points (A) and (B) on the interventricular septum are selected in the cross-sectional image along the *longitudinal* axis of the heart. The direction of the ultrasonic beam passing through the measurement points is selected to be almost perpendicular to the interventricular septum during the measurements. There may be, however, complex movement in the heart wall during the period of one heartbeat. Although the ultrasonic beam is perpendicular to the septum during the measurement in the cross-sectional image along the longitudinal axis, it is not guaranteed that the ultrasonic beam is perpendicular to the wall surface because it is probable that the ultrasonic beam tilts in the cross-sectional image along the short axis. Thus, the small vibration is also measured for the point selected in the cross-sectional image along the *short* axis of the heart and is compared with that for the *longitudinal* axis as follows. Fig. 18(c) and (d) shows the small vibrations $\{v_B(t)\}$ at the LV side of the interventricular septum of a presumedly healthy 22-year-old male volunteer, where the measured point B is selected in the cross-sectional image along the longitudinal axis and the short axis, respectively. The small vibration signals of six heartbeats are overlaid in each figure and the waveforms are shown for the period around the second heart sound in Fig. 18(a). Fig. 18(e) and (f) shows the average power spectra of the signals in Fig. 18(c) and (d), respectively. The average power spectra of the vibration signals for six heartbeats are shown by the solid lines. The minimum and maximum values of the vibration signals for six heartbeats are shown by the vertical bars for each frequency component in the power spectra. For the frequency components less than 80 Hz, the

vertical bar is very short, that is, sufficient reproducibility is obtained. The waveforms in Fig. 18(c) are similar to those in Fig. 18(d). At the same time, the power spectrum in Fig. 18(e) is also similar to that in Fig. 18(f). From these results, it is found that the ultrasonic beam is perpendicular to the wall plane of the interventricular septum during the measurements. Thus, the small vibration signal of the interventricular septum is measured with sufficient reproducibility by selecting the ultrasonic beam passing through the measured points so that it is perpendicular to the heart wall in the cross-sectional images along the conventional longitudinal axis or the conventional short axis of the heart.

VI. COMPARISON OF HEART WALL VIBRATIONS BETWEEN NORMAL SUBJECTS AND PATIENTS

Fig. 19 shows the waveforms of the small vibration signals on the LV side of the interventricular septum of three presumedly healthy young male volunteers and their average power spectra. The waveforms of several heartbeats are overlaid and shown at the moment of the emission of the second heart sound. The horizontal center in Fig. 19(a-1)–(c-1) corresponds to the moment of the emission of the second heart sound. For each subject, the reproducibility is quantitatively confirmed up to at least 100 Hz using the reproducibility function $|\hat{\gamma}_0(f)|^2$ of (28). For the power spectra, the employed lines are the same format as those in Fig. 18(e) and (f). By comparing Fig. 19(a-1)–(c-1) and (a-2)–(c-2), it can be seen that the waveforms and power spectra of these three volunteers are similar.

For three patients with acute lymphoblastic leukemia who have been treated with antracenadiones (mitoxantrone), the waveforms of the vibration signals on the LV side of the
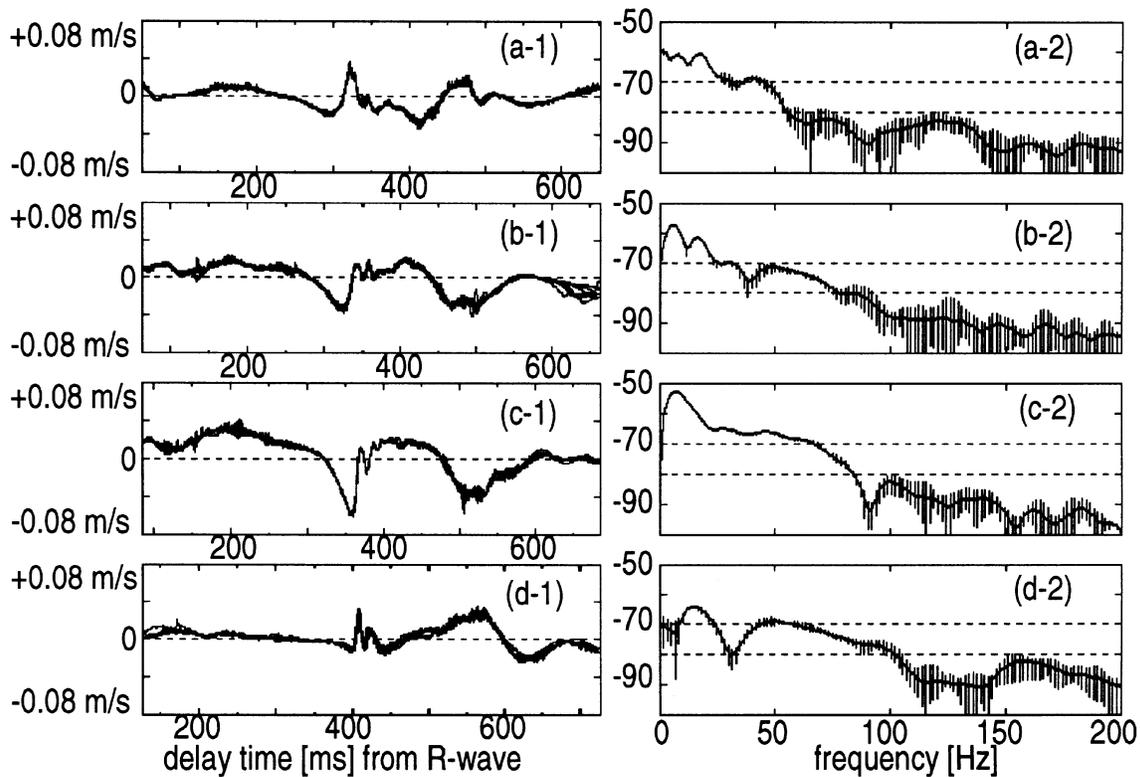
Fig. 20. The waveforms of the small vibration signals on the LV side of the interventricular septum for three patients with acute lymphoblastic leukemia who have been treated with antracenadiones (mitoxantrone), and their average power spectra. (a) A 32-year-old male patient; eight heartbeats overlaid; the measurement was performed two months before his death. (b) The same patient as (a); eight heartbeats overlaid; the measurement was performed three months before the measurement of (a). (c) A 23-year-old male patient; five heartbeats overlaid; this subject is also represented in Figs. 13–17. (d) A 25-year-old female patient; six heartbeats overlaid. For the waveforms of these patients, high-frequency components higher than 50 Hz are decreased.

interventricular septum and their average power spectra are shown in Fig. 20. The subject in Fig. 20(c) is the same as that represented in Figs. 13–17. The subjects in Fig. 20(c) and (d) are in complete remission. The subject in Fig. 20(b) was in the hospital. Three months after the measurement of the waveforms in Fig. 20(b), the waveforms in Fig. 20(a) were measured for the same patient. Then about two months after the last measurement, the subject died. For the four waveforms of these patients, the frequency components higher than 50 Hz are less as compared with the power spectra in Fig. 19. Especially for the waveforms in Fig. 20(a-1), only the low-frequency components less than 50 Hz are included. For the subject in Fig. 20(d-1), the components lower than 30 Hz are decreased. For the subject in Fig. 20(c-1), the power is still large for the frequency components up to 80 Hz. However, the waveforms during the isovolmetric relaxation period, which begins just after the moment of the second heart sound emission, are different from those for the healthy volunteers in Fig. 19.

To quantitatively evaluate the decrease of the vibration power of the patients from those of the healthy volunteers, three kinds of average power, P_1 dB from dc to 30 Hz, P_2 dB from 30 to 60 Hz, and P_3 dB from 60 to 100 Hz, are calculated from the average power spectra in Figs. 19 and 20.

The distribution of the resultant values of the average power, P_1, P_2, and P_3, is indicated by circles for the three healthy subjects and by x's for the patients in Fig. 21. As shown in
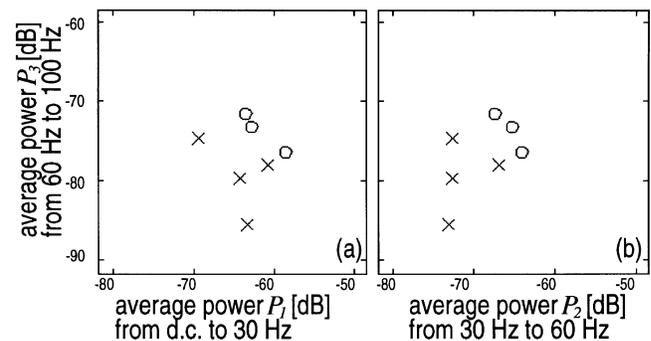

Fig. 21. Distribution of the three values of the average power, P_1 dB from dc to 30 Hz, P_2 dB from 30 to 60 Hz, and P_3 dB from 60 to 100 Hz for each patient, denoted by x's, of Fig. 20 and each healthy volunteer, denoted by circles, of Fig. 19. The power of the heart wall vibrations of patients is decreased by at least several dB in comparison with those of the healthy subjects.

Fig. 21, the power of the vibration of all patients is decreased by at least several dB as compared with that of the healthy subjects.

Myocardial physical properties have been reported to change sensitively under various pathological conditions. In a study using an *isolated* canine left ventricle with regional ischemia, the instantaneous impedance frequency curve [35] changed from a single-peak configuration to a double-peak configuration after the cessation of coronary flow and returned to the single-peak configuration with the recommencement of

coronary flow [36]. The difference between the power spectra in Fig. 19 and those in Fig. 20 corresponds to the changes in the acoustical characteristics of the local myocardium due to the injection of mitoxantrone. Mitoxantrone has been reported to have an adverse cardiotoxic effect, which results in irreversible diffuse myocardial fibrosis at cumulative or high doses.

Taking these experimental results into account, the method proposed in this paper provides a new approach to the detection of such myocardial physical and/or histological heterogeneity of a ventricle by analyzing human heart vibrations measured noninvasively from the chest surface.

VII. CONCLUSIONS

In this paper we have proposed a new method for accurate measurement of small *vibrations* on a large *motion* using ultrasound. Using a measurement system to realize this method, small vibrations were accurately measured in the frequency range up to 1 kHz in experiments using a water tank. By applying the method and the measurement system to the measurement of vibration signals of the interventricular septum in *in vivo* experiments, sufficient reproducibility was confirmed for the frequency components up to 100 Hz. With the system devised herein, it is possible to detect small vibrations up to 1 kHz. However, the amplitude of frequency components higher than 100 Hz in the *in vivo* experiment was too small to be measured accurately. The obtained change in thickness of the septum will directly relate to the regional contractility of the myocardium and it is diagnostic for ischemia and infarction. Discussion of the data on thickening and their implications will be presented in a separate paper in the near future.

Further investigation of this proposed method, including its clinical application to the noninvasive local diagnosis of coronary artery disease, drug-induced myocardial disease, and arteriosclerosis, is being conducted. It is necessary to identify the origin of and the process by which the heart wall vibrations detected in this paper were generated. In this paper, measured vibration signals are analyzed in the frequency domain only for the period around the second heart sound emission. It is also necessary to analyze the vibration signals for other periods.

APPENDIX A
NONCONSTRAINT LEAST-SQUARE APPROACH

This appendix describes the minimization of the normalized mean squared difference $\alpha_n(\beta_n, \delta_x)$ of (4). Equation (4) is simply rewritten as follows:

$$
\begin{aligned}
&\alpha_n(\beta_n; \delta_x) \\
&= \frac{\displaystyle\sum_{x \in R} |y(x + \delta_x; t + \Delta T) - \beta_n(\delta_x) y(x; t)|^2}{\displaystyle\frac{\sum_{x \in R} \{|y(x + \delta_x; t + \Delta T)|^2 + |y(x; t)|^2\}}{2}} \\
&= \frac{A(\delta_x) + B \cdot |\beta_n|^2 - C(\delta_x) \cdot \beta_n^* - C(\delta_x)^* \cdot \beta_n}{\dfrac{A(\delta_x) + B}{2}}
\end{aligned}
\tag{A1}
$$

where $*$ denotes the complex conjugate, $A(\delta_x)$ and B are a real function of δ_x and a real constant, respectively, defined by

$$
A(\delta_x) = \sum_{x \in R} |y(x + \delta_x; t + \Delta T)|^2 \tag{A2}
$$

$$
B = \sum_{x \in R} |y(x; t)|^2 \tag{A3}
$$

and $C(\delta_x)$ is a complex function of δ_x defined by

$$
C(\delta_x) = \sum_{x \in R} y^*(x; t) \cdot y(x + \delta_x; t + \Delta T). \tag{A4}
$$

Describing $C(\delta_x)$ and β_n by the sum of their real and imaginary parts, $C_R + jC_I$ and $\beta_{nR} + j\beta_{nI}$, respectively, the normalized mean squared difference $\alpha_n(\beta_n, \delta_x)$ in (A1), multiplied by $[A(\delta_x) + B]/2$, is described by

$$
\begin{aligned}
\frac{A(\delta_x) + B}{2} \cdot \alpha_n(\beta_n; \delta_x) = {}& A(\delta_x) + B \cdot (\beta_{nR}^2 + \beta_{nI}^2) \\
&- 2(C_R \beta_{nR} + C_I \beta_{nI}).
\end{aligned}
\tag{A5}
$$

By taking partial derivatives of $\alpha_n(\beta_n; \delta_x)$ with respect to β_{nR} and β_{nI} and setting them to zero

$$
\begin{aligned}
\frac{1}{2} \cdot \frac{A(\delta_x) + B}{2} \cdot \frac{\partial \alpha_n}{\partial \beta_{nR}} &= B \cdot \beta_{nR} - C_R \\
&= 0.
\end{aligned}
\tag{A6}
$$

$$
\begin{aligned}
\frac{1}{2} \cdot \frac{A(\delta_x) + B}{2} \cdot \frac{\partial \alpha_n}{\partial \beta_{nI}} &= B \cdot \beta_{nI} - C_I \\
&= 0.
\end{aligned}
\tag{A7}
$$

From (A6) and (A7)

$$
B \cdot \beta_n - C(\delta_x) = 0. \tag{A8}
$$

Thus

$$
\hat{\beta}_n = \frac{C(\delta_x)}{B}. \tag{A9}
$$

By substituting $\hat{\beta}_n$ of (A9) into (A1), the minimum value $\alpha_{n\,\text{MIN}}(\delta_x)$ of $\alpha_n(\beta_n; \delta_x)$ is given by

$$
\begin{aligned}
\alpha_{n\,\text{MIN}}(\delta_x) &\overset{\text{def}}{=} \min_\beta \alpha_n(\beta_n; \delta_x) \\
&= \frac{A(\delta_x) - \dfrac{|C(\delta_x)|^2}{B}}{\dfrac{A(\delta_x) + B}{2}}.
\end{aligned}
\tag{A10}
$$

Using the original signals $y(x, t)$ and $y(x + \delta_x; t + \Delta T)$, the minimum value $\alpha_{n\,\text{MIN}}(\delta_x)$ of $\alpha(\beta_n; \delta_x)$ in (A1) is obtained as follows:

$$
\alpha_{n\,\text{MIN}}(\delta_x) = \frac{\displaystyle\sum_{x \in R} |y(x; t)|^2 - \frac{\left|\displaystyle\sum_{x \in R} y^*(x; t) \cdot y(x + \delta_x; t + \Delta T)\right|}{\displaystyle\sum_{x \in R} |y(x; t)|^2}}{\dfrac{\displaystyle\sum_{x \in R} \{|y(x; t)|^2 + |y(x + \delta_x; t + \Delta T)|^2\}}{2}}.
\tag{A11}
$$

This equation is inferred by (6) of Section II-B.

APPENDIX B
DERIVATION OF THE VALUES OF THE CONSTANTS A, B, AND C

This appendix theoretically derives the values of $A(\delta_x)$ of (A2) and (C2), B of (A3) and (C3), and $C(\delta_x)$ of (A4) and (C4) for the simple model of (7) and (8) in Section II-B. The function $A(\delta_x)$ defined in (A2) and (C2) is obtained by

$$
A(\delta_x) = \sum_{x \in R} |y(x + \delta_x; t + \Delta T)|^2
$$
$$
= \sum_{n=0}^{N-1} |y_2(n + \delta_x)|^2
$$
$$
= \sum_{n=0}^{N-1} |z_0|^{2(n+n_0+\delta_x)} \cdot w(n + n_0 + \delta_x) \qquad \text{(B1)}
$$

where the range R is defined by $[0, N-1]$. For the case $n_0 + \delta_x < 0$

$$
A(\delta_x) = \sum_{n=-(n_0+\delta_x)}^{N-1} |z_0|^{2(n+n_0+\delta_x)}
$$
$$
= \sum_{n=0}^{N-1+n_0+\delta_x} |z_0|^{2n}
$$
$$
= \frac{1 - |z_0|^{2(N+n_0+\delta_x)}}{1 - |z_0|^2} \qquad \text{(B2)}
$$

while for the case $n_0 + \delta_x \geq 0$

$$
A(\delta_x) = \sum_{n=0}^{N-1} |z_0|^{2(n+n_0+\delta_x)}
$$
$$
= |z_0|^{2(n_0+\delta_x)} \frac{1 - |z_0|^{2N}}{1 - |z_0|^2}. \qquad \text{(B3)}
$$

For the constant B defined in (A3) and (C3)

$$
B = \sum_{x \in R} |y(x; t)|^2
$$
$$
= \sum_{n=0}^{N-1} |y_1(n)|^2
$$
$$
= \sum_{n=0}^{N-1} |z_0|^{2n}
$$
$$
= \frac{1 - |z_0|^{2N}}{1 - |z_0|^2}. \qquad \text{(B4)}
$$

The complex function $C(\delta_x)$ defined in (A4) and (C4) is given by

$$
C(\delta_x) = \sum_{x \in R} y^*(x; t) \cdot y(x + \delta_x; t + \Delta T)
$$
$$
= \sum_{n=0}^{N-1} y_1^*(n) \cdot y_2(n + \delta_x)
$$
$$
= \sum_{n=0}^{N-1} z_0^{*n} \cdot z_0^{(n+n_0+\delta_x)} \cdot w(n + n_0 + \delta_x). \qquad \text{(B5)}
$$

For the case of $n_0 + \delta_x < 0$

$$
C(\delta_x) = \sum_{n=-n_0-\delta_x}^{N-1} z_0^{*n} \cdot z_0^{(n+n_0+\delta_x)}
$$
$$
= \sum_{n=0}^{N-1+n_0+\delta_x} z_0^{*-(n_0+\delta_x)} \cdot |z_0|^{2n}
$$
$$
= z_0^{*-(n_0+\delta_x)} \frac{1 - |z_0|^{2(N+n_0+\delta_x)}}{1 - |z_0|^2} \qquad \text{(B6)}
$$

while for the case $n_0 + \delta_x \geq 0$

$$
C(\delta_x) = \sum_{n=0}^{N-1} |z_0|^{2n} \cdot z_0^{(n_0+\delta_x)}
$$
$$
= z_0^{(n_0+\delta_x)} \frac{1 - |z_0|^{2N}}{1 - |z_0|^2}. \qquad \text{(B7)}
$$

APPENDIX C
A CONSTRAINT LEAST-SQUARE APPROACH

This appendix describes the minimization of the normalized mean squared difference $\alpha(\beta, \delta_x)$ of (13) under the restriction that there is only a phase change between the signals $y(x; t)$ and $y(x; t+\Delta T)$. Equation (13) is simply rewritten as follows:

$$
\alpha(\beta; \delta_x) = \frac{\displaystyle\sum_{x \in R} |y(x + \delta_x; t + \Delta T) - \beta(\delta_x)y(x; t)|^2}{\dfrac{\displaystyle\sum_{x \in R} \{|y(x + \delta_x; t + \Delta T)|^2 + |y(x; t)|^2\}}{2}}
$$
$$
\qquad - \gamma[|\beta(\delta_x)|^2 - 1]
$$
$$
= \frac{A(\delta_x) + B \cdot |\beta|^2 - C(\delta_x) \cdot \beta^* - C(\delta_x)^* \cdot \beta}{\dfrac{A(\delta_x) + B}{2}}
$$
$$
\qquad - \gamma \cdot (|\beta|^2 - 1) \qquad \text{(C1)}
$$

where $A(\delta_x)$ and B are a real function of δ_x and a real constant, respectively, defined by

$$
A(\delta_x) = \sum_{x \in R} |y(x + \delta_x; t + \Delta T)|^2 \qquad \text{(C2)}
$$
$$
B = \sum_{x \in R} |y(x; t)|^2 \qquad \text{(C3)}
$$

and $C(\delta_x)$ is a complex function of δ_x defined by

$$
C(\delta_x) = \sum_{x \in R} y^*(x; t) \cdot y(x + \delta_x; t + \Delta T). \qquad \text{(C4)}
$$

Describing $C(\delta_x)$ and β by the sum of their real and imaginary parts, $C_R + jC_I$ and $\beta_R + j\beta_I$, respectively, the normalized mean squared difference $\alpha(\beta, \delta_x)$ in (C1), multiplied by $[A(\delta_x) + B]/2$, is described by

$$
\frac{A(\delta_x) + B}{2} \cdot \alpha(\beta; \delta_x)
$$
$$
= A(\delta_x) + B \cdot (\beta_R^2 + \beta_I^2) - 2(C_R\beta_R + C_I\beta_I)
$$
$$
\qquad - \frac{A(\delta_x) + B}{2} \cdot \gamma \cdot (\beta_R^2 + \beta_I^2). \qquad \text{(C5)}
$$

By taking partial derivatives of $\alpha(\beta; \delta_x)$ with respect to β_R, β_I, and γ and setting them to zero

$$\frac{1}{2} \cdot \frac{A(\delta_x) + B}{2} \cdot \frac{\partial \alpha}{\partial \beta_R} = B \cdot \beta_R - C_R$$
$$= 0 \qquad \text{(C6)}$$

$$\frac{1}{2} \cdot \frac{A(\delta_x) + B}{2} \cdot \frac{\partial \alpha}{\partial \beta_I} = B \cdot \beta_I - C_I$$
$$= 0 \qquad \text{(C7)}$$

$$-\frac{\partial \alpha}{\partial \gamma} = |\beta|^2 - 1$$
$$= 0. \qquad \text{(C8)}$$

From (C6) and (C7)

$$B \cdot \beta - C(\delta_x) - \frac{A(\delta_x) + B}{2} \cdot \gamma \cdot \beta = 0. \qquad \text{(C9)}$$

Thus

$$\beta = \frac{C(\delta_x)}{B - \dfrac{A(\delta_x) + B}{2} \cdot \gamma}. \qquad \text{(C10)}$$

By substituting (C10) into (C8)

$$\frac{|C(\delta_x)|^2}{\left[B - \dfrac{A(\delta_x) + B}{2} \cdot \gamma\right]^2} = 1 \qquad \text{(C11)}$$

because γ and B are real constants. Thus, the following quadratic equation is obtained:

$$\tfrac{1}{4}[A(\delta_x) + B]^2 \cdot \gamma^2 - [A(\delta_x) + B]B \cdot \gamma + B^2 - |C(\delta_x)|^2 = 0. \qquad \text{(C12)}$$

The solutions are given by

$$\gamma = \frac{2[B \pm |C(\delta_x)|]}{A(\delta_x) + B}. \qquad \text{(C13)}$$

By substituting these solutions of γ into (C10), the optimum values of β are obtained by

$$\beta_1 = -\frac{C(\delta_x)}{|C(\delta_x)|}$$
$$= \exp[-j\angle C(\delta_x)] \qquad \text{(C14)}$$
$$\beta_2 = \frac{C(\delta_x)}{|C(\delta_x)|}$$
$$= \exp[j\angle C(\delta_x)] \qquad \text{(C15)}$$

where $\angle C(\delta_x)$ denotes the phase of the complex function $C(\delta_x)$. From (C4) and (C15), (14) is obtained.

For β_1, the mean squared difference $\alpha(\beta, \delta_x)$ of (C1) is maximized, while for β_2, the minimization of $\alpha(\beta, \delta_x)$ is achieved. By substituting β_2 of (C15) and the relation of (C8)

into (C1), the minimum value $\alpha_{\text{MIN}}(\delta_x)$ of $\alpha(\beta; \delta_x)$ in (C1) is given by

$$\alpha_{\text{MIN}}(\delta_x) \overset{\text{def}}{=} \min_{\beta} \alpha(\beta; \delta_x)$$

$$= \frac{A(\delta_x) + B - \dfrac{2|C(\delta_x)|^2}{|C(\delta_x)|}}{A(\delta_x) + B}$$

$$= 1 - \frac{|C(\delta_x)|}{\dfrac{A(\delta_x) + B}{2}}. \qquad \text{(C16)}$$

Using the original signals $y(x, t)$ and $y(x + \delta_x; t + \Delta T)$, the minimum value $\alpha_{\text{MIN}}(\delta_x)$ of $\alpha(\beta; \delta_x)$ in (15) is given by

$$\alpha_{\text{MIN}}(\delta_x) = 1 - \frac{\left|\displaystyle\sum_{x \in R} y^*(x; t) \cdot y(x + \delta_x; t + \Delta T)\right|}{\dfrac{\displaystyle\sum_{x \in R} \{|y(x; t)|^2 + |y(x + \delta_x; t + \Delta T)|^2\}}{2}}. \qquad \text{(C17)}$$

This equation is inferred by (15) of Section II-D.

There is another procedure for this minimization of the normalized mean squared difference $\alpha(\beta; \delta_x)$ of (C1) under the restriction of $|\beta|^2 = 1$ as follows. By setting β to $\exp(j\theta)$, (C1) is described by the nonrestricted form as

$$\alpha(\beta; \delta_x)$$
$$= \frac{A(\delta_x) + B - C(\delta_x)\exp(-j\theta) - C(\delta_x)^*\exp(j\theta)}{\dfrac{A(\delta_x) + B}{2}}. \qquad \text{(C18)}$$

By taking partial derivatives of $\alpha(\beta; \delta_x)$ with respect to θ and setting it to zero

$$\frac{1}{2} \cdot \frac{A(\delta_x) + B}{2} \cdot \frac{\partial \alpha}{\partial \theta} = jC(\delta_x)\exp(-j\theta) - jC(\delta_x)^*\exp(j\theta)$$
$$= 0. \qquad \text{(C19)}$$

By multiplying (C19) by $\exp(j\theta)/j$

$$C(\delta_x) - C(\delta_x)^*\exp(j2\theta) = 0. \qquad \text{(C20)}$$

Thus, the optimum value of $\beta = \exp(j\theta)$ is given by

$$\hat{\beta} = \exp(j\hat{\theta})$$
$$= \pm\sqrt{\frac{C(\delta_x)}{C(\delta_x)^*}}$$
$$= \pm\frac{C(\delta_x)}{|C(\delta_x)|}. \qquad \text{(C21)}$$

$$\eta(f) = \frac{\displaystyle\sum_{i=1}^{M} |U_i(f) - U_0(f)|^2}{\displaystyle\sum_{i=1}^{M} |U_i(f)|^2} = \frac{\displaystyle\sum_{i=1}^{M} |U_i(f)|^2 - U_0(f)\sum_{i=1}^{M} U_i^*(f) - U_0^*(f)\sum_{i=1}^{M} U_i(f) + M|U_0(f)|^2}{\displaystyle\sum_{i=1}^{M} |U_i(f)|^2} \qquad \text{(D1)}$$

These two solutions are identical to those in (C14) and (C15). The form of this procedure is direct. In this paper, however, the constraint is explicitly described by introducing restriction of the second term into the right-hand side of (C1).

APPENDIX D
QUANTITATIVE EVALUATION OF REPRODUCIBILITY

To quantitatively evaluate the similarity of the M signals $\{u_i(t)\}$, $(i = 1, 2, \cdots, M)$ for each frequency component f, the normalized mean squared difference $\eta(f)$ of the spectrum $U_i(f)$ of $u_i(t)$ from the spectrum $U_0(f)$ of a waveform $u_0(t)$ is defined in (D1), as shown at the bottom of the preceding page, where M denotes the number of heartbeats. By taking a partial derivative of $\eta(f)$ with respect to $U_0^*(f)$

$$\frac{\sum_{i=1}^{M} |U_i(f)|^2}{2} \frac{\partial \eta(f)}{\partial U_0^*(f)} = -\sum_{i=1}^{M} U_i(f) + M \cdot U_0(f)$$
$$= 0. \quad \text{(D2)}$$

Thus, the optimum spectrum $U_0(f)$, which minimizes $\eta(f)$, is given by

$$\hat{U}_0(f) = \frac{1}{M} \sum_{i=1}^{M} U_i(f) \quad \text{(D3)}$$

which coincides with the average of $U_i(f)$ as a natural result. By substituting (D2) and the optimum $\hat{U}_0(f)$ of (D3) into $\eta(f)$ of (D1)

$$\hat{\eta}(f) = \frac{\sum_{i=1}^{M} |U_i(f)|^2 - \hat{U}_0(f) \sum_{i=1}^{M} U_i^*(f)}{\sum_{i=1}^{M} |U_i(f)|^2}$$
$$= 1 - \frac{\left| \sum_{i=1}^{M} U_i(f) \right|^2}{M \sum_{i=1}^{M} |U_i(f)|^2}. \quad \text{(D4)}$$

Let us define the reproducibility function, $|\gamma_0(f)|^2$, from the second term of the equation by

$$|\hat{\gamma}_0(f)|^2 = \frac{\left| \sum_{i=1}^{M} U_i(f) \right|^2}{M \sum_{i=1}^{M} |U_i(f)|^2}. \quad \text{(D5)}$$

Since $\hat{\eta}(f)$ has values from zero to one, the value of $|\hat{\gamma}_0(f)|^2$ is also from zero to one. If $|\hat{\gamma}_0(f)|^2$ is equal to one, M waveforms $\{u_i(t)\}$ completely coincide for the frequency component of f. If $|\hat{\gamma}_0(f)|^2$ is zero, there is no correlation between $\{u_i(t)\}$ for the frequency components of f.

REFERENCES

[1] H. Kanai, N. Chubachi, K. Kido, Y. Koiwa, T. Takagi, J. Kikuchi, and T. Takishima, "A new approach to time-dependent AR modeling of signals and its application to analysis of the fourth heart sound," *IEEE Trans. Signal Processing,* vol. 40, pp. 1198–1205, May 1992.
[2] S. Satomura, "Ultrasonic Doppler method for the inspection of cardiac function," *J. Amer. Soc. Acoust.,* vol. 29, no. 11, pp. 1181–1185, Nov. 1957.
[3] D. W. Baker, "Pulsed ultrasonic Doppler blood-flow sensing," *IEEE Trans. Sonics Ultrason.,* vol. SU-17, pp. 170–185, July 1970.
[4] F. D. McLeod and M. Anliker, "A multiple-gate pulsed directional Doppler flowmeter," in *Proc. IEEE Ultrason. Symp.,* Miami, FL, Dec. 1971.
[5] S. L. Johnson, D. W. Baker, R. A. Lute, and H. T. Dodge, "Doppler echocardiography," *Circulation,* vol. XLVIII, pp. 810–822, Oct. 1973.
[6] F. E. Barber, D. W. Baker, A. W. C. Nation, D. E. Strandness, Jr., and J. M. Reid, "Ultrasonic duplex echo-Doppler scanner," *IEEE Trans. Biomed. Eng.,* vol. BME-21, pp. 109–113, Mar. 1974.
[7] C. J. Hartley, H. G. Hanley, R. M. Lewis, and J. S. Cole, "Synchronized pulsed Doppler blood flow and ultrasonic dimension measurement in conscious dogs," *Ultrasound Med. Biol.,* vol. 4, pp. 99–110, 1978.
[8] M. Brandestini, "Topoflow—A digital full range Doppler velocity meter," *IEEE Trans. Sonics Ultrason.,* vol. SU-25, pp. 287–293, Sept. 1978.
[9] E. Wildi, J. W. Knutti, H. V. Allen, and J. D. Meindl, "Dynamics and limitations of blood/muscle interface detection using Doppler power returns," *IEEE Trans. Biomed. Eng.,* vol. BME-27, pp. 565–573, Oct. 1980.
[10] W. D. Barber, J. W. Eberhard, and S. G. Karr, "A new time domain technique for velocity measurements using Doppler ultrasound," *IEEE Trans. Biomed. Eng.,* vol. BME-32, pp. 213–229, Mar. 1985.
[11] C. Kasai, K. Namekawa, A. Koyama, and R. Omoto, "Real-time two-dimensional blood flow imaging using an autocorrelation technique," *IEEE Trans. Sonics Ultrason.,* vol. SU-32, pp. 458–463, May 1985.
[12] R. M. Olson and D. K. Shelton, "A nondestructive technique to measure wall displacement in the thoracic aorta," *J. Appl. Phys.,* vol. 32, no. 1, pp. 147–151, Jan. 1972.
[13] R. M. Olson and J. P. Cooke, "A nondestructive ultrasonic technique to measure diameter and blood flow in arteries," *IEEE Trans. Biomed. Eng.,* vol. BME-21, pp. 168–171, 1974.
[14] J. O. Arndt, "The diameter of the intact carotid artery in man and its change with pulse pressure," *Pflüegers Arch.,* vol. 301, pp. 230–240, 1968.
[15] D. J. Mozersky, D. S. Sumner, D. E. Hokanson, and D. E. Strandness, Jr., "Transcutaneous measurement of the elastic properties of the human femoral artery," *Circulation,* vol. XLVI, pp. 948–955, Nov. 1972.
[16] A. P. G. Hoeks, C. J. Ruissen, P. Hick, and R. S. Reneman, "Transcutaneous detection of relative changes in artery diameter," *Ultrasound Med. Biol.,* vol. 11, no. 1, pp. 51–59, 1985.
[17] W. T. Kemmerer, R. W. Ware, H. F. Stegall, J. L. Morgan, and R. Kirby, "Blood pressure measurement by Doppler ultrasonic detection of arterial wall motion," *Surgery, Gynecology, Obstetrics,* vol. 131, pp. 1141–1147, Dec. 1970.
[18] K. Lindström, K. Marsal, G. Gennser, L. Bengtsson, M. Benthin, and P. Dahl, "Device for measurement of fetal breathing movements, 1. The TD-recorder. A new system for recording the distance between two echogenetic structures as a function of time," *Ultrasound Med. Biol.,* vol. 3, pp. 143–151, 1977.
[19] D. E. Hokanson, D. E. Strandness, Jr., and C. W. Miller, "An echo-tracking system for recording arterial wall motion," *IEEE Trans. Sonics Ultrason.,* vol. SU-17, pp. 130–132, July 1970.
[20] D. E. Hokanson, D. J. Monzersky, S. D. Sumner, and D. E. Strandness, Jr., "A phase-locked echo tracking system for recording arterial diameter changes *in vivo*," *J. Appl. Phys.,* vol. 32, no. 5, pp. 728–733, May 1972.

[21] K. Nakayama and S. Sato, "Ultrasonic measurement of arterial wall movement utilizing phase-tracking system," in *Dig. 10th Int. Conf. Med. Biol. Eng.,* Dresden, 1973, p. 318.

[22] D. N. White and R. J. Stevenson, "Transient variations in the systolic pulsations in amplitude of intracranial echoes, their artificial origin," *Neurology,* vol. 26, pp. 683–689, 1976.

[23] C. F. Olsen, "Doppler ultrasound: A technique for obtaining arterial wall motion parameters," *IEEE Trans. Sonics Ultrason.,* vol. SU-24, pp. 354–358, June 1977.

[24] L. W. Korba, R. S. C. Cobbold, and A. J. Cousin, "An ultrasonic imaging and differential measurement system for the study of fetal respiratory movements," *Ultrasound Med. Biol.,* vol. 5, pp. 139–149, 1979.

[25] I. Rapoport and A. J. Cousin, "New phase-lock tracking instrument for foetal breathing monitoring," *Med. Biol. Eng. Comput.,* vol. 20, pp. 1–6, Jan. 1982.

[26] D. H. Groves, T. Powalowski, and D. N. White, "A digital technique for tracking moving interfaces," *Ultrasound Med. Biol.,* vol. 8, no. 2, pp. 185–190, 1982.

[27] C. J. Hartley, H. Litowitz, R. S. Rabinovitz, W. X. Zhu, J. E. Chelley, L. H. Michael, and R. Bolli, "An ultrasonic method for measuring tissue displacement: Technical details and validation for measuring myocardial thickening," *IEEE Trans. Biomed. Eng.,* vol. 38, pp. 735–747, Aug. 1991.

[28] L. S. Wilson and D. E. Robinson, "Ultrasonic measurement of small displacements and deformations of tissue," *Ultrason. Imag.,* vol. 4, pp. 71–82, 1982.

[29] C. J. Hartley, L. A. Latson, L. H. Michael, C. L. Seidel, R. M. Lewis, and M. L. Entman, "Doppler measurement of myocardial thickening with single epicardial transducer," *Amer. J. Physiol.,* vol. 245, pp. H1066–1072, 1983.

[30] A. P. G. Hoeks, P. J. Brands, F. A. M. Smeets, and R. S. Reneman, "Assessment of the distensibility of superficial arteries," *Ultrasound Med. Biol.,* vol. 16, no. 2, pp. 121–128, 1990.

[31] H. C. Andrews and B. R. Hunt, *Digital Image Restoration.* Englewood Cliffs, NJ: Prentice-Hall, 1977, pp. 148–150.

[32] H. Kanai, H. Satoh, K. Hirose, and N. Chubachi, "A new method for measuring small local vibrations in the heart using ultrasound," *IEEE Trans. Biomed. Eng.,* vol. 40, pp. 1233–1242, 1993.

[33] J. A. Cadzow and O. M. Solomon, Jr., "Linear modeling and the coherence function," *IEEE Trans. Acoust., Speech, Signal Processing,* vol. ASSP-35, pp. 19–28, 1987.

[34] A. A. Luisada and D. M. MacCanon, "The phases of the cardiac cycle," *Amer. Heart J.,* vol. 83, pp. 705–711, 1972.

[35] Y. Koiwa, R. Hashiguchi, T. Ohyama, S. Isoyama, S. Satoh, H. Suzuki, and T. Takishima, "Measurement of the instantaneous viscoelastic properties by impedance frequency curve of the ventricle," *Amer. J. Physiol.,* vol. 245, pp. H672–H684, 1986.

[36] R. Hashiguchi, Y. Koiwa, T. Ohyama, T. Takagi, J. Kikuchi, J. P. Butler, and T. Takishima, "Dependence of instantaneous transfer function on ischemic myocardial volume," *Circ. Res.,* vol. 63, pp. 1003–1011, 1988.

Hiroshi Kanai (A'88–M'91) was born in Matsumoto, Japan, on November 29, 1958. He received the B.E. degree from Tohoku University, Sendai, Japan in 1981, and the M.E. and the Dr.Eng. degrees, also from Tohoku University, in 1983 and 1986, both in electrical engineering.

From 1986 to 1988, he was with the Education Center for Information Processing, Tohoku University, as a Research Associate. From 1990 to 1992, he was a Lecturer in the Department of Electrical Engineering, Faculty of Engineering, Tohoku University. Since 1992, he has been an Associate Professor in the Department of Electrical Engineering, Faculty of Engineering, Tohoku University. His present interest is in ultrasonic measurements and digital signal processing for diagnosis of the heart diseases and arteriosclerosis.

Dr. Kanai is a member of the Acoustical Society of Japan, the Institute of Electronics Information and Communication Engineering of Japan, the Japan Society of Mechanical Engineers, the Japan Society of Ultrasonics in Medicine, the Japan Society of Medical Electronics and Biological Engineering, the Institute of Electrical Engineers of Japan, and the Japanese Circulation Society.

Michie Sato was born in Toyama, Japan, on November 30, 1972. She received the B.E. degree from Tohoku University, Sendai, Japan in 1995 in electrical engineering. Since 1995, she has been pursuing the Master's degree in electrical and communication engineering, Tohoku University, Japan.

Her current interest is in digital signal processing and ultrasonic measurement for cardiovascular disease.

Miss Sato is a member of the Acoustical Society of Japan and the Institute of Electrical Engineers of Japan.

Yoshiro Koiwa was born in Sendai, Japan, in 1944. He graduated from Tohoku University, Sendai, Japan, in 1969. He received the M.D. degree from Tohoku University in 1977.

He is presently an Associate Professor of Internal Medicine at Tohoku University. His main research interest is cardiovascular disease, especially cardiac function and heart failure.

Dr. Koiwa is member of the American Federation for Clinical Research, the Japanese Circulation Society, and the Japan Society of Medical Electronics and Biological Engineering.

Noriyoshi Chubachi (M'83) was born in Kokura, Japan, on October 5, 1933. He received the B.S., M.S., and Ph.D. degrees in electrical engineering from Tohoku University, Sendai, Japan, in 1956, 1962, and 1965, respectively.

In 1965 he joined the Research Institute of Electrical Communication, Tohoku University, where he was an Associate Professor from 1966 to 1978. Since 1979, he has been a Professor in the Department of Electrical Engineering, Tohoku University. From 1982 to 1983, he was a Visiting Professor of Electrical and Computer Engineering, University of California, Santa Barbara. He has worked on ultrasonic transducers and delay lines, surface acoustic devices, acoustoelectronics, piezoelectric materials, acoustic microscopy, and related problems.

Dr. Chubachi is a member of the Acoustical Society of America, the Institute of Electronics and Communication Engineers of Japan, the Society of Japanese Applied Physics, the Acoustical Society of Japan, the Japan Society of Ultrasonics in Medicine, the Japan Society for Nondestructive Inspection, the Japan Society of Medical Electronics and Biological Engineering, the Japan Society of Mechanical Engineers, and the Institute of Electrical Engineers of Japan. He served as Chairman, Tokyo Chapter of the IEEE Ultrasonics, Ferroelectrics, and Frequency Control Society from 1987 to 1988. He is currently serving as Vice President of the Acoustical Society of Japan.